Development of a turbulent separated flow validation test case: Experimental and computational (RANS) studies

Madeline Cary Samuell

A thesis
submitted in partial fulfillment of the
requirements for the degree of

MASTER OF SCIENCE IN AERONAUTICS & ASTRONAUTICS

University of Washington

2020

Reading Committee:

Owen J. H. Williams, Chair

Antonino Ferrante, Chair

Program Authorized to Offer Degree:
College of Engineering,
William E. Boeing Department of Aeronautics and Astronautics

University of Washington

Abstract

Development of a turbulent separated flow validation test case: Experimental and computational (RANS) studies

Madeline Cary Samuell

Co-Chairs of the Supervisory Committee:
Research Assistant Professor Owen J. H. Williams
Aeronautics & Astronautics

Associate Professor Antonino Ferrante
Aeronautics & Astronautics

A new validation test case for CFD of turbulent separated flows is investigated through a combination of experiments and simulations. This work is part of an ongoing collaboration between the University of Washington and Boeing, which aims to contribute to the development of a high-quality validation test case for turbulent separated flows and the improvement of RANS modeling for turbulent separated flows. A three-dimensional speed-bump-like geometry, which causes separation as a result of the surface curvature, was chosen for this study. Tests were conducted to determine the influence of Reynolds number and confinement on the flowfield and to test the ability of common RANS turbulence models to accurately predict the flow. Experimental data was used to formalize the required inflow length so that the bump inflow matched between the simulations and experiments. The parameter used to match the inflows was the Reynolds number based on momentum thickness, Re_θ, of the incoming boundary layer. The experimental data collected from the incoming boundary layer was also used to prove that the flow upstream of the bump was fully turbulent for all levels of confinement. Five Reynolds numbers were tested in the experiments and the simulations, corresponding to a freestream velocity range of 60 m/s - 20 m/s and four vertical confinement levels were analyzed in the experiments. Six turbulence models were examined:

$k-\omega$ SST, two versions of Spalart-Allmaras (SA and SARC) and three versions of $k-\epsilon$. The geometry was determined to be a challenge to RANS models, which was demonstrated by the pressure coefficient data because the simulations predicted an opposite Reynolds number trend to the experiments in the separated region. Furthermore, the simulations were not able to predict distinctive pressure coefficient profiles seen in the experimental results, such as an inflection point along the streamwise centerline in the separated region and a double-peak in the spanwise direction across the top of the bump. However, the simulations did predict that the flowfield is insensitive to Reynolds number at and above $Re_L = 2.46 \times 10^6$, which is in agreement with the Reynolds number insensitivity determined experimentally. Increasing confinement increased the magnitude of the pressure coefficients over the bump, and the pressure at the peak of the bump went from about -1.2 in the least confined case to about -1.5 in the most confined case. However, there was no change in the shape of the profile. The examination of the various RANS turbulence models concluded that, for this curved geometry, the turbulence models with the curvature correction, $k-\omega$ SST and SARC, corresponded more closely to the experimental flow than those without a curvature correction. None of the $k-\epsilon$ models predicted separation, but SARC, SA and $k-\omega$ SST all did. It was determined that SARC, SA and $k-\omega$ SST all displayed similar flow features to those observed in the experimental flow visualizations, such as the general shape of the separated region and counter-rotating surface vortices that were symmetric across the streamwise centerline. However, the extent, location and width of the separated region varied. Along with variation in the size of the separation bubble predicted by each turbulence model, they also all predicted different values and profiles for pressure and skin friction coefficient in the separated region. From this experimental and computational analysis, it is clear that this geometry poses a sufficient challenge to current RANS models, due to their inability to accurately predict the location, size and values of pressure coefficients within the separated region. Therefore, is a good choice for a turbulent separated flow validation test. Future

work on this project will focus on detailed flowfield comparisons between experiments and simulations.

TABLE OF CONTENTS

LIST OF FIGURES

NOMENCLATURE

u: streamwise velocity

U_∞: freestream velocity

x: streamwise coordinate

y: spanwise coordinate

z: wall-normal coordinate

p: pressure

δ: distance from wall where the velocity reaches $0.99U_\infty$

δ^*: displacement thickness

θ: momentum thickness

ρ: fluid density

τ_w: wall shear stress

u_τ: friction velocity = $\sqrt{\tau_w/\rho}$

Re_θ: Reynolds number based on momentum thickness

Re_τ: Reynolds number based on friction velocity

Re_x: Reynolds number based on streamwise distance

C_f: skin friction coefficient = $\tau_w/(0.5\rho U_\infty^2)$

C_p: pressure coefficient

μ: fluid dynamic viscosity

h: bump height

H: distance from top of splitter plate to tunnel ceiling

L: wind tunnel width (36")

L_b: width of splitter plate (35.5")

z^+: non-dimensional wall normal distance based on friction velocity

ACKNOWLEDGMENTS

I am incredibly grateful to my co-advisors, Dr. Owen Williams and Dr. Antonino Ferrante, for giving me the opportunity to be involved in this project, and for providing guidance and support every step of the way.

I also would like to thank Boeing for sponsoring and collaborating with us on this project, especially Jeff Slotnick and Dr. Philippe Spalart.

To Abhiram Aithal, thank you for always being there to help me with my computational research. You taught me so much and I cannot thank you enough.

To Matt Robbins and Sage Sarwas, I am so grateful to have worked with both of you on the experimental side of this project. You made stressful weeks fun and this thesis could not have come together without you.

I would like to thank my undergraduate advisor from Union College, Dr. Ann Anderson, for inspiring me to pursue this graduate degree.

Finally, to my family and friends, thank you for your love and support. You mean the world to me and I would not be where I am without you.

DEDICATION

This thesis is dedicated to my parents and my sister. Thank you for always believing in me, supporting all of my dreams, and being there for me whenever I needed you.

Chapter 1

INTRODUCTION

Computational fluid dynamics (CFD) is an indispensable tool in the field of fluid dynamics because it enables researchers to analyze and collect data in great detail on all flow variables. Surface measurements, such as skin friction and pressure coefficients on the body of an object, flowfield visualizations and calculations of the flowfield turbulence kinetic energy (TKE) are just some of the many possibilities. CFD results must be validated against experimental data because many simulations, with the exception of direct numerical simulation (DNS) rely on models to close the complex Navier-Stokes equation in order for them to be solvable. These models solve approximate versions of the governing equations because solving the full equations, as in the case of DNS, is a very large computational expense. Reynolds numbers of engineering systems are typically too large for DNS, making modeling necessary because DNS is only feasible for flows with low Reynolds numbers and relatively simple geometries. Though modeling is heavily relied on in CFD, the approximate models are not accurate for all flow conditions. More experimental data is needed to improve models and make them more accurate over a wide range of flows. One of the most common modeling methods used are the Reynolds-averaged Navier-Stokes (RANS) equations, which solve for the time averaged flow. RANS simulations require a turbulence model to close the equations. There are many turbulence models available and they have each been developed for specific flow regimes and to accurately model certain flow behaviors, therefore the type of flow condition should determine which turbulence model is used.

The prevalence of, and reliance on, CFD in the aerospace industry has continued to increase over recent decades. The high Reynolds number and complex geometry in most aerospace CFD simulations preclude the use of DNS. Therefore, RANS models are widely

used in the aerospace industry. While RANS turbulence models can perform well in most flow regimes when appropriately tuned and validated, there are flow regimes where they are not so reliable. One such regime is turbulent separated flow, which occurs often on stalled airfoils and aerodynamic bodies that are maneuvering or at high angles of attack. Improving models in this flow condition would have a significant impact on the aircraft design process because turbulent separated flow has some severe negative repercussions, such as loss of lift and increase in aerodynamic drag. RANS models typically struggle to correctly predict the separation point and tend to have further difficulty identifying the reattachment point [6]. Using improved and reliable RANS models, designers could study where turbulent separation is occurring and, in some cases, delay or mitigate separation. Therefore, improved RANS models could lead to improved designs of aerodynamic bodies by enabling designers to devote more attention to the details in the separated regions that current RANS models cannot capture.

NASA published a report in 2014, "CFD Vision 2030," which outlined the steps necessary to significantly advance CFD capabilities [7]. In this report, an emphasis was placed on improving RANS models for turbulent separated flow and the development of new high-quality validation experiments. CFD simulations must be validated against experimental data from tests that are carefully conducted, with stringent documentation of uncertainties, instrumentation and results. These experiments are called validation test cases, and their data is made public for anyone to access. Validation experiments are difficult to produce because meeting the requirements of a high-quality validation test case, outlined by Oberkampf and Smith [8], is sometimes infeasible for projects. This is because the understanding and characterization of uncertainties for flowfield variables and boundary conditions is now more stringent than ever before and is often beyond the characterization undertaken for experiments that have been used for validation in the past. While producing a validation test case is a goal of this project, this is a long term goal. The datasets included in this thesis are not yet at the level required for a validation test case. Widely publicizing turbulent separated flow validation data that can meet the requirements of Oberkampf and Smith would give people developing

and testing new turbulence models the ability to determine if they are matching the data with uncertainty and for the correct reasons. It is currently difficult to determine which turbulence model is better for a certain flow condition and why.

The research discussed in this thesis is part of a larger collaboration between Boeing, the University of Washington and other university and research partners around the world. This group seeks to answer the call laid out in the "CFD Vision 2030" report by developing a turbulent separated flow validation test case and conducting experiments and CFD simulations to examine the turbulent flow over this geometry.

The shape chosen for this study needed to produce a turbulent separated flow which challenged the current RANS model. The ability to precisely manufacture and simulate the geometry was taken into consideration. For simulations, the shape needed to be conducive to grid generation. Furthermore, complexities like three-dimensionality and sidewall interactions needed to be minimized and a smoothly varying curvature was necessary to ensure that the separation and reattachment were not determined by any surface discontinuities. A speed-bump-like geometry was chosen, as it satisfied the above criteria. It is described by a Gaussian curved in the streamwise direction and in the spanwise direction, it has a uniform midsection before tapering at the shoulders, which is defined by an error function.

The focus of this thesis is the experiments carried out in the University of Washington's $3' \times 3'$ wind tunnel and the CFD simulations developed to compare to the experimental results. The influences of Reynolds number and confinement on the flowfield were investigated experimentally. The simulations were also used to study the effect of Reynolds number and additionally to conduct a turbulence model sensitivity study using common RANS turbulence models. Surface pressure measurements and boundary layer measurements were conducted in the wind tunnel for five freestream velocities (20 m/s, 30 m/s, 40 m/s, 50 m/s and 60 m/s) to determine the sensitivity to Reynolds number, and four levels of confinement in the vertical direction for the flow confinement sensitivity study. Simulations were carefully developed to ensure that the incoming boundary layer matched the experimental boundary layer. Comparison between the experiments and simulations were primarily done

using surface pressure coefficients, surface flow visualizations and incoming boundary layer profiles.

The three overarching goals in this research were to (1) determine if the bump geometry is a stringent test of current RANS turbulence models, (2) examine the sensitivity to Reynolds number and confinement and (3) identify the regions of the flow where the RANS turbulence models have the most disagreement. The turbulence model sensitivity study, was conducted to meet the first goal by comparing experimental and computational surface flow visualizations and surface pressures. If all the turbulence models examined resulted in data that perfectly matched the experimental data, this geometry would not be a good test of the RANS models. Having computational data that did not perfectly match the experimental data meant that the models break down at some point in the domain and are unable to accurately predict the experimental flow. Understanding where this breakdown occurs and what the models predict (instead of the actual behavior) will offer insight into why the models are failing and, potentially, how they can be improved. Examining the sensitivity to Reynolds number was done experimentally and computationally by varying the freestream velocity. This us helpful in understanding how the data collected in this project might scale up to large aerospace applications with much higher Reynolds numbers. If the results appeared to be Reynolds number insensitive, then the trends seen here would be applicable to a wide range of aerospace applications. The same is true for the purpose of the confinement study that was conducted experimentally. These two studies would also deepen the knowledge about this flow and it's behavior, which would be beneficial for anyone trying to improve or develop RANS models for turbulent separated flow. The final goal, identifying regions of flow that change with different turbulence models, was investigated using surface streamlines and contours of pressure and skin friction. This is critical to understand the strengths and weaknesses of each turbulence model and how that translates to turbulent separated flow.

To ensure that the simulation domain was well defined, the confinement of the sidewalls and top wall in the computational domain was developed to match the confinement in the wind tunnel test section. Then, the inflow was analyzed to confirm that the incoming

simulation boundary layer matched the experimental incoming boundary layer. Finally, simulations were conducted to ensure that the outflow was sufficiently long enough to not have an influence on the results. Grid development was an important consideration for the CFD study as the grid can introduce uncertainty into the results [6]. A grid convergence study was conducted to ensure that the gridding was also well-defined and validated. For this study, the number of grid points in the streamwise, spanwise and vertical direction were varied, as well as the refinement at the walls. During this convergence study, special attention was paid to the z^+_{min} and y^+_{min}, which are the non-dimensional distances of the first grid point from the plate and sidewalls, respectively, to ensure there was a high level of resolution within the boundary layer.

The results of the studies conducted for this thesis show that well-defined simulations with a validated and optimized grid were developed and that these simulations were well-matched to the experiments. Furthermore, current RANS simulations do not accurately predict the flow in separated regions. In fact, Reynolds number trends observed in the separated regions were opposite to that of the experiments and the shape of the surface pressure profiles along the streamwise and spanwise centerlines of the bump geometry were not the same between the simulations and experiments, particularly in the separated region. It was also determined that some turbulence models are better able to predict the flow than others, with some of them failing to predict any separation at all. Between the turbulence models that did predict separation, there was very little agreement regarding the shape and size of the separated region or the location of separation and reattachment.

Chapter 2

BACKGROUND & THEORY

2.1 Challenge of Turbulent Separated Flows

Turbulent separation is a common flow phenomenon that occurs when fluid becomes detached from the surface it is traveling over. Detachment means that the surface shear stress goes to zero, creating recirculating flow, which is the separated region. Separation is described as the departure or breakdown of the boundary layer flow and it results in the appearance of a near-wall rotational region and an increase in the velocity component normal to the wall [9]. Attached flow is easier to simulate and model because the shear stress in the streamwise direction is the only turbulence statistic that must be taken into account, though three-dimensional flows become more complicated because there are two shear stress components [1]. The shear stress affects many aspects of the flow, such as the skin friction coefficient, the relationship between the outer flow and the boundary layer displacement thickness, and the momentum deficit in the wake. Modeling this type of flow accurately is more feasible than separated flow because there is only one variable to determine, the shear stress, and the changes are mainly happening, typically slowly, in the direction of the flow. Separated flow, particularly the separation and reattachment points, is much more difficult to characterize because the entire turbulence structure affects the flow. Separation and reattachment are also highly coupled with the dynamics of the shear layer and recirulation. Furthermore, the detaching boundary layer no longer follows the log-law model and there are no known universal functions to describe, and subsequently simplify, its behavior [10]. The boundary layer must be fully resolved and this also involves all the complex turbulent stresses. The turbulence in the separated shear layer that eventually begins to reattach is changing and evolving throughout the flow, which makes reattachment complicated as well. All of these

challenges are present for two-dimensional flow, but there are additional ones for three-dimensional separated flow, making those even more difficult to model.

Turbulent separation that occurs over aircraft surfaces at high angles of attack, like flaps, wings, undercarriage etc., during takeoff and landing is particularly challenging for CFD simulations to model because the aerodynamically smooth bodies do not have a separation location that is defined by the geometry. A backward facing step geometry produces a separated flow, but the separation location is defined by the geometry. It occurs at the step every time. For a aerodynamically curved, smooth geometry, the point of flow separation is not set by the geometry so the location changes based on characteristics of the flow, such as the Reynolds number, incoming boundary layer and freestream turbulence. The presence of a pressure gradient, which is always present on any real vehicle, adds additional challenges.

Separation leads to acoustic noise and pressure fluctuations, which cause additional loading and fatigue on the aircraft. Flow devices that experience separated flow also undergo a performance reduction, leading to lower fuel efficiency as a result of loss of lift and increased drag [9]. A better understanding of turbulent separation would enable researchers and designers to investigate and test ways to control or delay separation, which would mitigate the negative results. Separation is common on an aircraft at the edges of the flight envelope (i.e. at the limits of the aircraft's ability), which is already where the most uncertainties related to the aircraft exist. Predicting separation would help define the edges of the flight envelope.

A report published by NASA in 2014, called the "CFD Vision 2030 Study," called for improved computational models of turbulent separated flow and improved validation test cases for these types of flows [7]. It particularly highlights the need to improve the capability and accuracy of RANS models. In this report, a list of barriers and technology gaps were developed to determine why the models are so inaccurate for these types of flows at present. The list includes, but is not limited to, the lack of improvements to the models based on physics from fundamental validation and calibration datasets, inadequate use and availability of turbulent separated flow experiments over curved geometry to validate models, limited collaboration between turbulence researchers, both experimental and computational, and

limited in-depth understanding and development of pre-separation physics modeling. Improving CFD models is important because the aerospace industry has come to rely on them because, as the NASA report states, they, "enable reductions in ground-based and in-flight testing requirements, but also provide added physical insight, enabl[ing] superior designs at reduced cost and risk, and open[ing] new frontiers in aerospace vehicle design and performance." Using DNS would theoretically solve the issues presented by using RANS models, but DNS is infeasible for nearly all aerospace applications due to the high level of computational expense it would require. Large eddy simulation (LES), which directly solves for the large scales in the flow and models the smaller scales, would also provide more accurate results than the RANS models, but it is also too expensive for most aerospace applications. Therefore, given the significant role that CFD plays in the aerospace industry, it is necessary to focus on development and advancement of RANS models.

The "CFD Vision 2030" report places emphasis on validation test cases for turbulent separated flow because, in order to validate the performance of modified or improved RANS turbulence models, the results must be compared to experimental data of the same, or similar, flow type. Furthermore, this data must come from an experiment that carefully minimizes and documents any error or uncertainties. The requirements for a validation test case are increasingly stringent, requiring an exceptionally high level of capabilities for testing facilities in order to fully satisfy said requirements [8]. After developing and conducting these high quality validation experiments, the datasets would be made available to the public to provide researchers with a reliable comparison for their own turbulent separated flow simulations.

2.2 Reynolds-Averaged Navier-Stokes(RANS)

The discussion in the previous section highlighted the importance of RANS models to CFD and the aerospace industry, and the need to further develop these models so they are more accurate for turbulent separated flows. Their inaccuracy leads to their inability to predict the separation and reattachment points over aerodynamically smooth surfaces, as well as the trends in a turbulent separated flow. The primary challenge in modelling separated flows

is a result of the rapidly changing turbulence in the flow and the complicated strain fields that are present in both two-dimensional and three-dimensional separating flow [1]. Existing models are able to more accurately model separation when the detachment point is set by the geometry, but separation over a curved surface is much more difficult. This struggle with separation over curved surfaces is what the "CFD Vision 2030 Study" identified and called for improvement [7]. Fig. 2.1 gives examples of a number of separated flows discussed in a 2004 paper by Leschziner et. al. that explored the challenges of modeling separated flows for aerodynamic applications.

Each turbulence model has its own strengths and flaws, therefore the appropriate turbulence model is dependent on the characteristics of the flow to which is it being applied. Four turbulence models will be discussed in this thesis: Spalart-Allmaras (SA), Spalart-Allmaras with a curvature correction (SARC), $k-\omega$ SST and $k-\epsilon$.

The Spalart-Allmaras (SA) model is a one-equation eddy viscosity turbulence model solving a turbulent viscosity transport equation. It is particularly applicable for boundary layers with pressure gradients, which makes it popular for use in aerodynamic flows. However, it has difficultly capturing the flow of a backward-facing step and handling reattachment behind a shock wave under an adverse pressure gradient [11]. SARC is the same turbulence model, modified to perform better for curved surfaces.

The $k-\omega$ SST turbulence model is a two-equation eddy viscosity model. This model is known to accurately simulate turbulent boundary layers, backward-facing steps and flow that undergoes moderate separation [12]. Though similar in structure to $k-\epsilon$, given that they are both two-equation eddy viscosity models, its performance and the flows it is more accurately able to predict are much more similar to SA. Due to this similarity, $k-\omega$ SST is also a good choice for aerospace applications [13].

As stated in the above paragraph, $k-\epsilon$ is a two-equation eddy viscosity turbulence model. It originally was developed in order to improve upon the mixing-length model [14]. This model is known to perform poorly for adverse pressure gradients because it overestimates the shear stress and tends to predict a separation point downstream of the actual separation

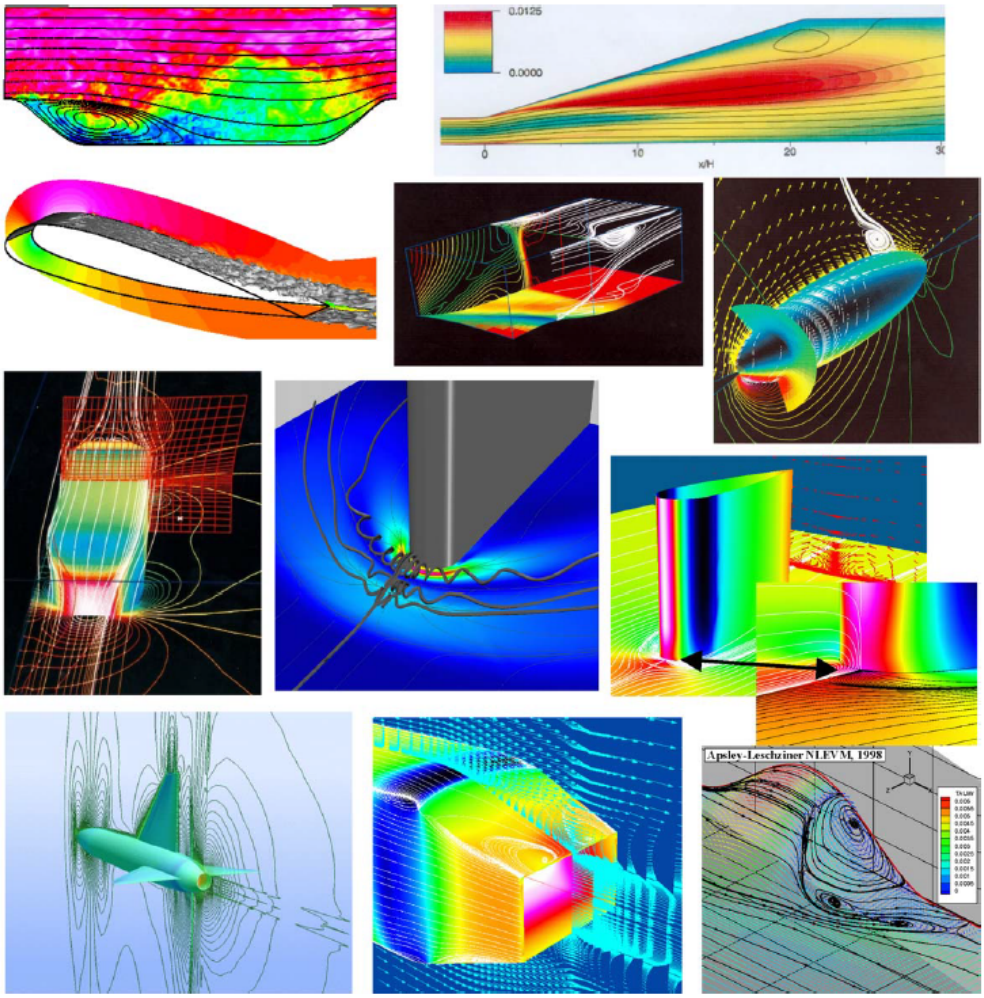

Figure 2.1: Examples of separated flow simulations investigated in the paper by Leschziner et. al. [1].

point. In some cases $k-\epsilon$ will not predict any separation when separation is known to occur according to other models and experiments [15]. It underestimates separation because $k-\epsilon$ has a tendency to be overly diffusive in boundary layers with an adverse pressure gradient. This is because, in the near wall region, $k-\epsilon$ overestimates the turbulent length scale and viscosity, resulting in overly high predictions of the skin friction coefficient [1].

Though SA, SARC and $k-\omega$ SST are known to be able to model mild separation to an extent, they struggle with accurately predicting the locations of separation and reattachment [1]. These models typically predict long and thin separated regions. The mild success of these models is because they were developed for wall boundary layers. Therefore if these models are adapted for boundary layers with adverse pressure gradients, they can capture some rough characteristics of the separated region. However, estimations are not enough to predict separation and define the edges of the flight envelope. Therefore, the accuracy and reliability of CFD must be increased in order to increase its efficacy in the aerospace industry.

2.3 Turbulent Separated Flow Studies

2.3.1 Previous Studies

Turbulent separated flow studies have been conducted both experimentally and computationally within the last few decades. Some of these studies focus on flow that separates as a result of an imposed pressure gradient [16], while others focus on separation that is a result of surface curvature. Some of these past studies have been focused on separation over two-dimensional geometries [17, 2], while others have looked at three-dimensional axisymmetric geometries [18, 3, 19, 20, 4]. The two-dimensional studies, though more simple to analyze, were not able to examine sidewall interactions or streamline-divergence effects. In some of the three-dimensional studies, the geometry controlled the separation location. In order to challenge the RANS turbulence models, it is necessary to use a geometry that does not have a specific location where separation occurs every time. The goal is to have a separation

location that is dependent on the flow characteristics and test whether these turbulence models are able to predict that separation location. Furthermore, while some of these studies involved comparison to CFD simulation results [21, 4], many focused on the physics of turbulent separation [18, 17, 16, 3, 19, 20]. Specific validation test cases with meticulous and in-depth comparison to CFD studies are required to improve the RANS models. Fig. 2.2 includes examples of geometries used in a number of the previous validation studies.

While some of the past studies reported tunnel qualifications [3, 18], they did not report the full extent of requirements necessary for a level 2 or 3 validation experiment, as laid out by Oberkampf and Smith [8]. These requirements include spatial and temporal measurements to highly resolve things like the freestream inflow, the near wall inflow, outflow characteristics, and boundary and initial conditions of both the wind tunnel test section and the model in the test section. All of these listed items fall under the *Boundary and Initial Conditions* category. The other five categories identified by Oberkampf and Smith are: *Experimental Facility*, *Analog Instrumentation and Signal Processing*, *Fluid and Material Properties*, *Test Conditions*, and *Measurement of System Responses*. There are four completeness levels: 0, 1, 2, and 3. Each category is assessed based on its individual requirements and if the experiment meets all of them, it is considered level 3. To be considered a good validation experimental, call categories should be level 2 or 3. All of these previous studies have contributed greatly to the understanding of the dynamics and physics of separated flows, but to make steps to improve the RANS models, more focus must be placed on high quality validation experiments of turbulent separated flows with thorough comparison to, and validation of, matching CFD simulations.

2.3.2 Current Studies

An ongoing collaboration between a number of researchers at Virginia Tech and NASA is developing a turbulent separated flow validation test case using a three-dimensional, axisymmetric bump, with the intention of reaching Oberkampf and Smith level 3 in all categories [5]. The test geometry is shown in Fig. 2.3. It features a flat section on the top that gives

the boundary layer a chance to recover after the favorable pressure gradient on the upstream slope. This project is a direct response to the call for improved RANS modeling, outlined in the "CFD Vision 2030" study. Their goal is to use Particle Image Velocimetry (PIV) with hot-wire anemometry, skin friction measurements, flow visualization techniques and surface pressure measurements to develop a complete and well-documented dataset. Large Eddy Simulation (LES) and RANS simulations are being conducted simultaneously to determine their ability to accurately predict the flow. The experiments and simulations are matched using inflow parameters such as the Reynolds number based on the momentum thickness (Re_θ), Reynolds number based on the height, h, of the bump (Re_h), the ratio of bump height to the incoming boundary layer thickness, δ, in a specified location upstream of the bump (h/δ) and the ratio of the bump height to the momentum thickness, θ, upstream of the bump (h/θ). The simulations used $k-\omega$ SST, SA, SARC and $k-\epsilon$ turbulence models to determine each model's ability to accurately predict the flow. Three-dimensional CFD results showed that $k-\omega$ SST model matched the experimental surface pressure distribution more accurately than SA. However, both models were unable to match the pressure distribution in the separated region. PIV measurements have shown that flow separates on the upstream side of the bump, and the size of this separation bubble is dependent on Reynolds number. With the exception of the upstream slope, the flow was determined to be Reynolds number insensitive [22]. This project plans to conduct more in-depth experimental tests to produce a high quality validation dataset and more simulations to further investigate the geometry's sensitivities and the capabilities of various CFD models.

A CFD validation study of a transonic hump is currently being conducted at Sandia National Laboratories [23]. These experiments are based on the past work of Bachalo and Johnson [20] and examine an unsteady, transonic flow over an axisymmetric spherical bump. The flow becomes supersonic at the top of the bump and undergoes unsteady separation before reattaching downstream. The validation experiment will include data from PIV, oil flow surface visualization, high speed Schlieren to track the shock location and motion, and oil film interferometry to calculate the surface shear stress. No CFD comparisons are being

run by the Sandia National Lab researchers, but there is an open call to the community to use the provided geometry, incoming flow parameters and boundary conditions to simulate the same flow so that the ability of current CFD models to predict unsteady, transonic flows can be analyzed.

2.4 Boeing/UW Gaussian Bump Turbulent Separated Flow Validation Geometry

A new validation test geometry has been proposed in a UW-Boeing collaboration, aiming to build upon previous work and avoid both modeling and data validation challenges. The project discussed in this thesis will investigate flow behavior over a three-dimensional bump experimentally and computationally and develop the experiments alongside the simulations to gain a more complete understanding of the uncertainties. An additional goal is to satisfy all the requirements for a level 2 validation experiment, which is the highest level for a validation test, as described by Oberkampf and Smith [8].

The geometry chosen for these tests needed to be possible to manufacture with accuracy for the wind tunnel experiments and also easy to generate a computational grid for the simulations. It had to produce a turbulent separated flow, meaning the boundary layer had to be turbulent and fully developed before reaching the geometry in the wind tunnel. While separation was a necessity, the separation point could not be defined by a single point in the geometry, like a sharp edge, such as in a backward facing step, instead, the extent of separation should be controlled by varying geometric and flow parameters. The geometry should minimize sidewall interactions. Flow confinement in a wind tunnel test is unavoidable, so confinement should be incorporated into the definition of the tests for accurate comparison between experiments and simulations.

The geometry that was chosen resembles a speed bump. It is defined by the function shown in Eqn. 2.1, which is Gaussian in the streamwise direction. In the spanwise direction, the middle section of the geometry is uniform before tapering down to the sidewalls. The tapering at the shoulders is defined by an error function. The streamwise and spanwise

centerlines are plotted in Fig. 2.4.

$$z(x,y) = \frac{h_0}{2} e^{-\left(\frac{x}{x_0}\right)^2} \left[1 + erf\left(\frac{\frac{L_b}{2} - 2y_0 - |y|}{y_0}\right)\right] \tag{2.1}$$

The important geometric parameters included in the function describing the bump (eqn. 2.1) are L_b, the width of the splitter plate (35.5"). The width of the wind tunnel, L, is 36". Other parameters used to define the geometry are $x_0 = 0.195L_b$, $y_0 = 0.06L_b$, and $h_0 = 0.085L_b$, the latter of which is the height of the bump.

This geometry was selected for relative ease of manufacture and simulation, as described above, but also because it would have quasi two-dimensional behavior along the streamwise centerline and three-dimensional behavior around the shoulders. This three-dimensionality provides a challenge for the RANS turbulence models, but tapering at the sidewalls minimizes the complicated sidewall interactions. The geometry is wider in the spanwise direction than it is long in the streamwise direction, making it more applicable to aerospace applications due to its loose resemblance to an airplane wing. The geometry is symmetric on either side of the streamwise centerline, which helps with the uncertainty quantification.

This three-dimensional geometry is unique compared to the others used in validation studies for turbulent separated flow, such as the hill-type models [3, 19, 18] or the model currently being studied by Virginia Tech [5] because it has a more wing-like shape and relatively thinner upstream boundary layer.

In collaboration with this project, researchers at the University of Colorado, Boulder and Boeing Commercial Airplanes looked at turbulent separation over a two-dimensional Gaussian bump [24]. Direct numerical simulation (DNS) and wall-modeled large eddy simulation (WMLES) were both conducted in this study. The SA and $k-\omega$ RANS closures were selected for WMLES. On the downstream side of the bump, where separation occurred, the solution was highly dependent on the RANS model. The Reynolds number of the flow was $Re_\theta = 1000$ at the inflow and the boundary layer thickness was 1/8 the height of the bump. The skin friction coefficient is predominantly determined by the ability of the RANS model to capture the near-wall physics and pressure gradients, which poses a great challenge to

current RANS models. This study determined that both the SA and $k-\omega$ SST models were unable to accurately predict the flow in the favorable pressure gradient region of the domain, which occurs on the bump leading up to the peak.

This thesis will expand upon previous work conducted by Sage Sarwas and discussed in their Master's thesis [25] and further work which was presented at the AIAA SciTech 2020 Forum [26]. The previous work focused on the experiments, including design of equipment, freestream turbulence quantification in the wind tunnel, proof that the inflow boundary layer was turbulent upstream of the bump, and the first set of experimental results; surface flow visualization, surface pressure measurements and boundary layer measurements. All simulations discussed in previous work were initial results and were purely two-dimensional. This thesis focuses on the development of the three-dimensional simulations. CFD and experimental studies were conducted to determine the effect of the Reynolds number on the extent of separation and an additional confinement study was conducted experimentally at four different levels of vertical confinement. A CFD turbulence model study was conducted to determine the abilities of four common turbulence models (SA, SARC, $k-\omega$ SST and $k-\epsilon$) to accurately predict the flow. Finally, surface streamlines plotted from the simulation results were compared to the surface flow visualization results previously discussed in Sage Sarwas' thesis and the SciTech 2020 paper on this topic [25, 26]. The work outlined in this thesis was done to determine whether the bump geometry chosen is a thorough and precise test of the RANS turbulence models, test the sensitivity to Reynolds number and confinement and examine the performances of the common RANS models and the regions of the flow where they illicit the most different results.

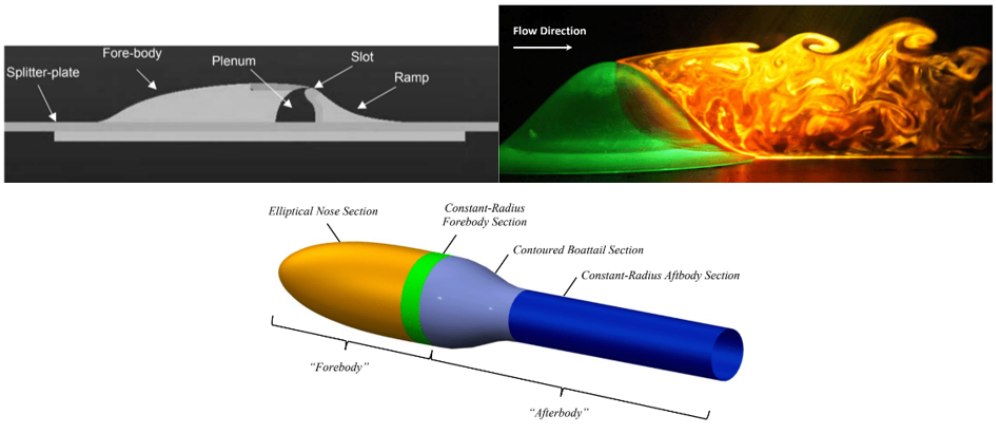

Figure 2.2: Geometries from previous turbulent separated flow validation studies. They are (top left) a two-dimensional wall-mounted hump, (top right) the FAITH hill model, and (bottom) a three-dimensional axisymmetric afterbody [2, 3, 4].

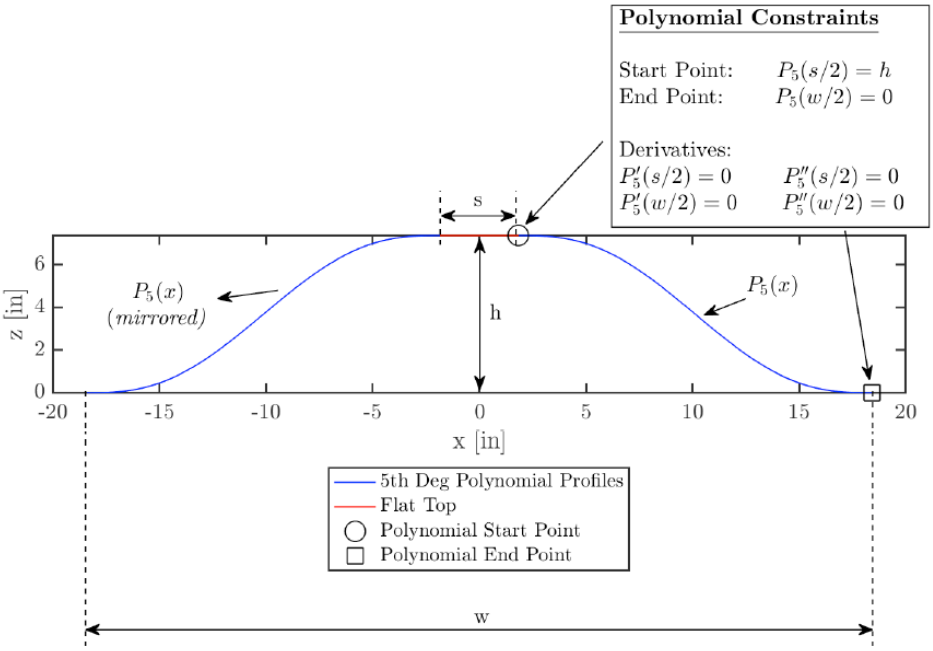

(a)

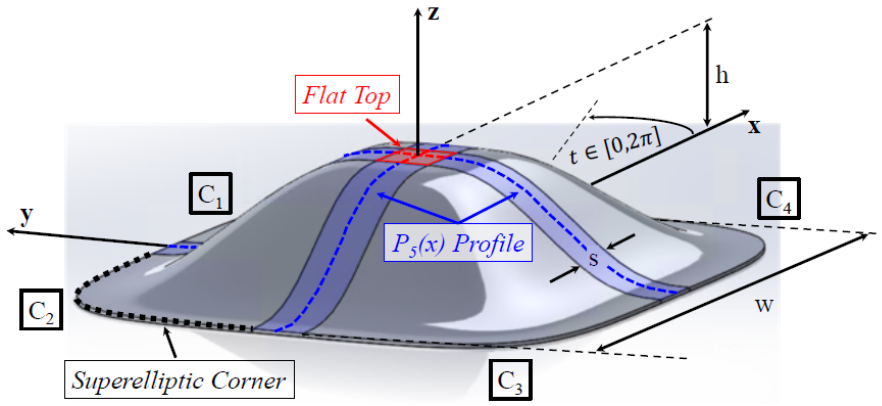

(b)

Figure 2.3: Model of the three-dimensional axisymmetric bump used in the Virginia Tech/NASA benchmark experiments for CFD validation [5].

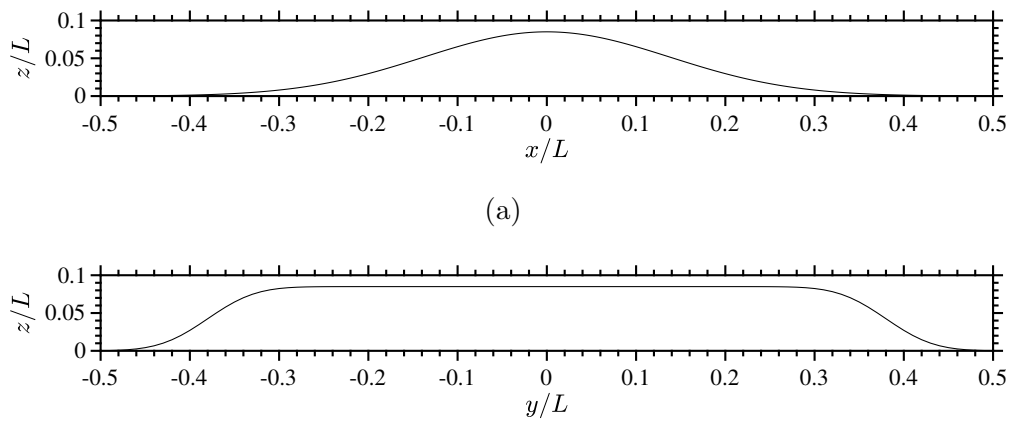

Figure 2.4: Geometry of bump model in (a) streamwise and (b) spanwise directions relative to wind tunnel test section width, L.

Chapter 3

EXPERIMENTAL AND COMPUTATIONAL SETUP

There were two components to this research: experimental work that was conducted at the University of Washington's 3' x 3' low-speed wind tunnel and computational work that was conducted in Star-CCM+. The experimental work included measurement of the incoming mean velocity profile and surface pressure measurements. A mechanical traverse was installed in the plate upstream of the bump to measure the incoming boundary layer. Surface pressure measurements were acquired using pressure taps placed along the streamwise centerline on the plates upstream and downstream of the bump. On the bump itself, pressure taps were scattered in a grid pattern, with the majority placed on the downstream side of the bump to capture the pressures in the separated region.

Computational fluid dynamics (CFD) simulations were conducted with the same geometry in Star-CCM+, a commercial CFD software. A number of RANS simulations were conducted in order to test the capability of the turbulence models to accurately predict the measured flow and to determine if the selected geometry is a good test of the current RANS turbulence models. Simulation and experimental results were compared using surface pressure coefficients, inflow velocity profiles and surface streamlines. Additional simulations were conducted to analyze the geometry's sensitivity to different parameters, such as the Reynolds number and the turbulence model.

3.1 Wind Tunnel and Test Geometry Configuration

The 3' x 3' wind tunnel in the Aerodynamics Laboratory at the University of Washington, is an open return tunnel with a maximum velocity of 60 m/s. It features a 3' x 3' x 8' test section with Plexiglas walls. The tunnel has a 200 HP, constant speed motor with pneumatically

actuated variable pitch blades. Flow uniformity in the test section is controlled by the 9:1 inlet contraction, three screens and a honeycomb section. Running the tunnel causes a significant increase in the room temperature, therefore no tests were started until the temperature in the room reached an equilibrium. The temperature in the building can be controlled by opening up vents to the ambient air outside the building. The flow quality was analyzed and determined to be uniform, with freestream turbulence intensities of 0.2% across the velocity range of 10 m/s - 60 m/s. A picture of the facility is shown in Fig. 3.1.

3.2 Experimental Methodology and Setup

The speed-bump-like geometry was mounted on an aluminum splitter plate and the whole configuration could be moved up or down to different vertical locations in the tunnel to increase or decrease the confinement. The vertical positions were $H/L = 1/2, 5/12, 1/3, 1/4$. The initial configuration was with the upper surface of the splitter plate at $H/L = 1/2$ from the ceiling of the tunnel. The splitter plate and bump setup were bolted to two steel frames that were pinned to the sidewalls of the tunnel. The aluminum splitter plate was MIC-6 Aluminum. The surface roughness was $0.5\mu m$, which was critical so that the boundary layer developed properly. The maximum deviation of the plate from being truly flat was $0.127mm$.

The leading edge of the plate featured an 8-inch long, 3D printed modified super ellipse to ensure a smooth laminar flow at the beginning of the plate, upstream of the artificial trip. The artificial trip was placed at the location where the leading edge joined with the aluminum plate, which was $1L$ from the peak of the bump. A number of tripping devices were tested, three different sandpapers (240-grit, 120-grit and 60-grit) as well as velcro. Each trip tested produced a turbulent boundary layer, but the boundary layer produced was relatively independent of the trip used, meaning the larger artificial trips produced nearly the same boundary layer as the smaller ones. The smallest grit sandpaper, 240-grit, was selected. For more detail regarding the tests conducted to select the trip, see the Master's Thesis written by Sage Sarwas [25]. A summary of this work is also included in the paper that was presented at the SciTech conference in Orlando, FL in January 2020 [26].

Figure 3.1: UW 3' x 3' low speed wind tunnel where experimental tests for this research were conducted. The clear test section can be seen in towards the back of the image.

A 12-inch trailing edge flap was attached at the end of the splitter plate. The angle of this flap could be adjusted using a turnbuckle to ensure that the leading edge stagnation point was at or above the geometric leading edge of the plate. To determined the stagnation point location, two sets of two 1/32" static pressure taps were placed on the top and bottom of the leading edge surface, 0.5" from the start of the surface, on either side of the streamwise centerline. The pressure difference between the taps on the top and bottom surface was used to determined the location of the stagnation point. It was determined that a trailing edge flap angle of 8 degrees was the minimum possible angle that ensured the stagnation point was on the top surface. Fig. 3.2 shows a schematic of the bump and splitter plate and a CAD rendering of the set up in the wind tunnel is shown in Fig. 3.3.

The upstream and downstream aluminum plates both featured two insert positions where the probe traverse mechanism that was designed to measure the boundary layer could be inserted. When the traverse was not inserted in the plate, an aluminum stopper, made of the same aluminum as the plate, was inserted into the opening. The stopper was flush with the surface, causing no effect on the flow.

The bump was constructed by Steven Seim of CyberModelle using epoxy and ATH powder. The bump has a maximum wall thickness of 0.5". This hollow design was chosen for the pressure taps that were drilled all over the bump surface. The bump is bolted to an aluminum plate using six 3/8" bolts. The backing plate and the upstream and downstream aluminum plates all feature joints that overlap and bolt together. The bump and backing plate had the same thickness as the upstream and downstream plates at the joints, 0.75", therefore there was a smooth transition from the plate to the bump and back. Speed tape covered the seam between the two sections. Fig. 3.4 shows images of the setup in the wind tunnel looking upstream and downstream.

Pressure taps were used to measure the pressure coefficient over the surface of the bump and along the streamwise centerline upstream and downstream, nine of which were on the plates and 40 on the bump for a total of 49 pressure taps. The largest concentration of pressure taps was placed downstream of the peak of the bump to increase resolution in

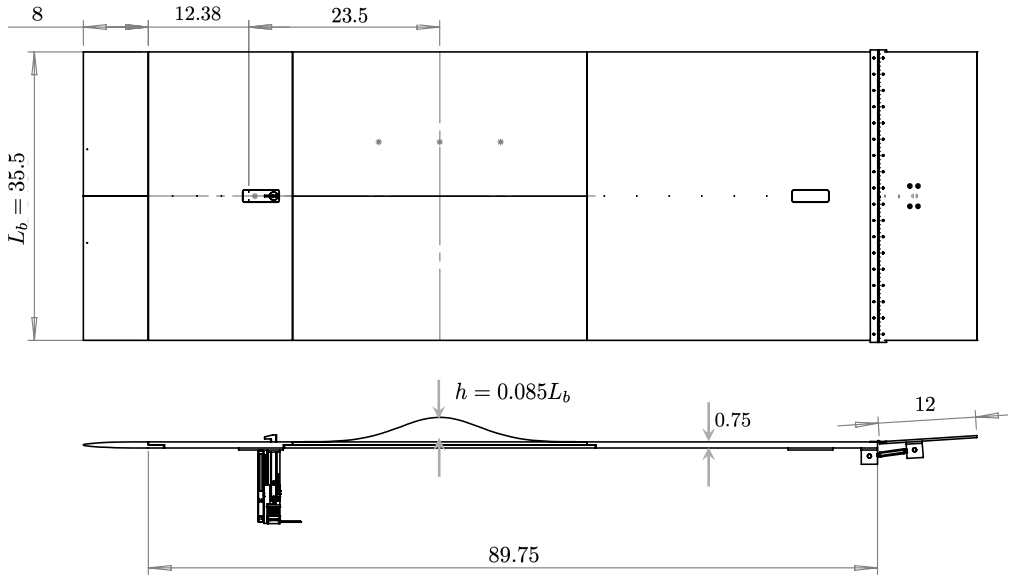

Figure 3.2: Schematic of splitter plate, its three main sections, leading edge and trailing edge flap. A 0.25" gap is left between the plate and tunnel walls on each side. This is filled with neoprene rubber strips to prevent leakage around the edges of the plate. All dimensions in inches. The trips were located at the joint between the leading edge and first plate section.

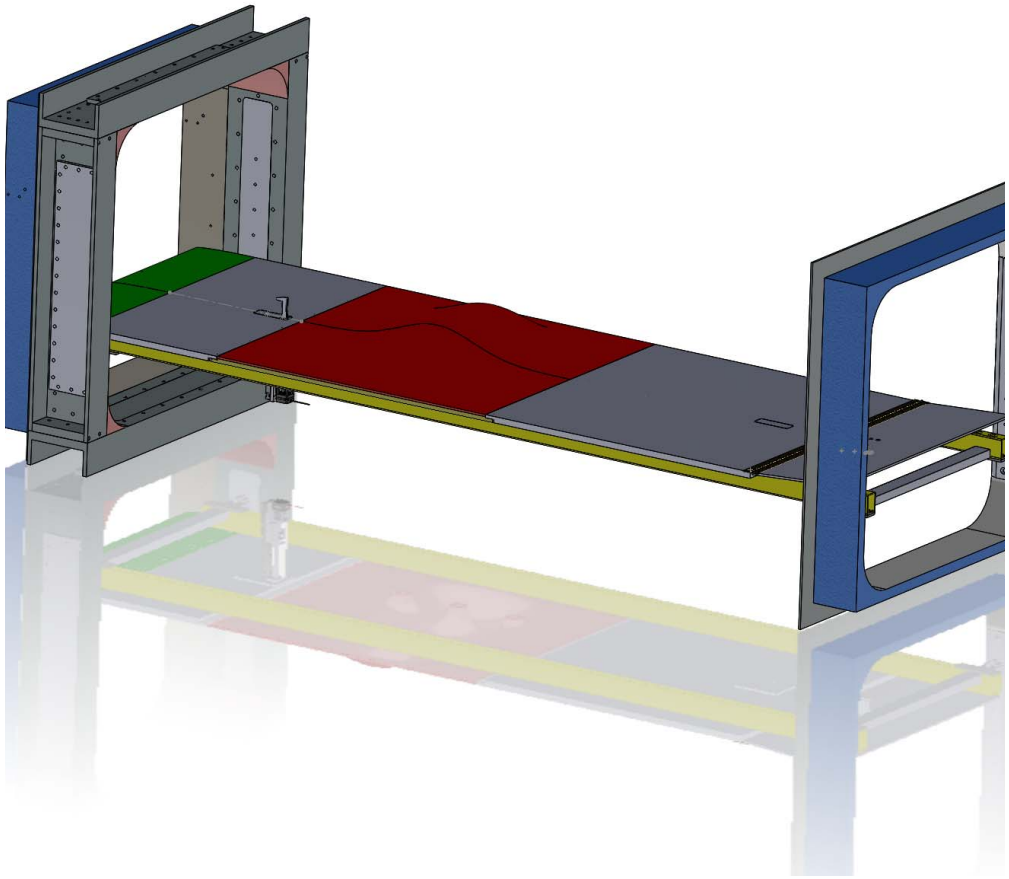

Figure 3.3: Full assembly showing the bump (in red), leading edge (in green) and splitter plate, mounted to the brackets in the tunnel.

the separated region. The pressure taps were 1/32"-diameter and were drilled normal to the surface. Clear plastic tubing was attached to the taps on the underside of the bump, which ran to a Scanivalve and an external pressure transducer to take the measurements. A diagram of the location of all the pressure taps is shown in Fig. 3.5. The first tap on the upstream plate, labeled 0, was used as the reference tap to which the other pressures were compared. The spanwise pressure taps were symmetrically placed about the centerline to determine if there were any biases present in the span.

There were six vertical locations, called stations, where the plate and bump configuration could be bolted to the side of the tunnel, $H/L = 2/3, 7/12, 1/2, 5/12, 1/3, 1/4$. The centerline case, $H/L = 1/2$, is station 4. Station 1 is the one with the most confinement with $H/L = 1/4$ and station 6 is the one with the least confinement with $H/L = 2/3$.

3.2.1 Boundary Layer Measurements

The incoming boundary layer was measured using a traverse that was inserted into the slot cut out of the plate upstream of the bump. The traverse had a pitot tube mounted on it, pointing upstream, and two reference pressure taps on the base of the traverse, flush with the surface of the plate. The reference taps went to the reference side of a differential pressure transducer and the pitot tube went to the other. The pressure data collected by the pitot tube was used to calculate the boundary layer velocity profile, the momentum thickness (θ), and the boundary layer thickness (δ). The boundary layer measurement location was $0.65L$ upstream of the peak of the bump, which was also $0.35L$ downstream of the start of the leading edge.

The pitot probe diameter was 0.02". This small diameter was necessary to get as close to the wall as possible to properly measure the thin boundary layer. The probe was mounted on a slide that moved perpendicular to the wall through a low friction PTFE slot. The probe's motion was controlled by a Velmex UniSlide lead screw and a LIN Engineering 417 stepper motor. The traverse was controlled by a labview script that enabled the user to define a set number of points to measure in the boundary layer and their location from the wall. As the

traverse moved up, it would stop at each one of these defined positions to collect data, before moving onto the next position. A Heidenhain SlimLine LS477 linear encoder was mounted to the slide to control the location of the steps. The encoder had a step resolution of $0.5\mu m$. For more details regarding the design, manufacturing and components of the traverse, refer to Sage Sarwas' Master's thesis [25].

For each boundary layer test, a calibration had to be conducted to determine how far off the surface of the plate the probe started. This was because the exact starting position could not be exactly defined with each test, leading to small discrepancies in the starting locations for each boundary layer measurement. Macro-photography was used to determine this starting wall distance, by taking a photo of the probe at the beginning of the test with a high-resolution Nikon DSLR camera. Probe dimensions visible in the photo, as well as the reflection of the probe on the aluminum surface and the number of pixels in the photo, were used as a reference to determine the probe's distance off the wall. This offset distance was taken into consideration when plotting the boundary layer profile and determining the important boundary layer parameters (momentum thickness, boundary layer thickness, etc.).

3.2.2 Surface Pressure Measurements

Surface pressure measurements were initially taken using a Baratron 226A differential pressure transducer, with a range of 20 Torr and accuracy of 0.50%. A Scanivalve solenoid was used to measure all of the pressure taps sequentially, one by one. The Baratron transducer is a differential transducer that compares one pressure to a reference pressure. The first upstream tap on the streamwise centerline, located on the aluminum plate, was used as the reference pressure and all subsequent taps were compared to that one. Unfortunately, in a few of the higher Reynolds number cases the measured pressure was up against the range of the Baratron and the measurement was cut off. This problem worsened for the high Reynolds numbers in the cases where the confinement was increased. To correct this issue, a new pressure transducer was chosen for the cases where the cutoff occurred. The new Baratron transducer was also 226A with an accuracy of 0.50%, but this one had a 50 Torr

range instead of a 20 Torr range. Therefore, for the lower velocity and lower confinement cases, the 20 Torr Baratron was used and for the high velocity and higher confinement cases, the 50 Torr Baratron was used.

The full range of Reynolds numbers based on the width of the bump, L, (Re_L) from 1.32×10^6 - 3.41×10^6 were tested. These values of Re_L correspond to freestream velocities of 20 m/s - 60 m/s. Another sensitivity that was examined in addition to Reynolds number was confinement. For the purposes of this research, surface pressure measurements were taken at stations 1-4 ($H/L = 1/4 - 1/2$).

3.3 Development of Simulations

The two primary steps in the process of setting up the CFD simulations used in this research were (1) selecting the appropriate models and setting up the physics of the flow and (2) generating a suitable and efficient grid. The goal of this project was to challenge RANS simulations, but the various RANS turbulence models have a significant impact on the results, even if everything else is held the same.

On the grid side, the computational domain used for the simulations needed to contain the same geometry as the experiments and have matching (or in the case of the inflow and outflow, similar) dimensions. A domain was generated around the bump geometry and the height and width of the domain were originally defined as $L/2$ and L, respectively.

The inflow length was more complicated to define because the boundary layer in the experiments was artificially tripped, which is not done in the simulations. If the simulation inflow length was defined to be the same as the experimental inflow length, the incoming boundary layers would not match. Instead, the inflow length was adjusted to ensure that, at the specified boundary layer measurement location, $0.65L$ in front of the peak of the bump, the experimental and simulation boundary layers matched. The two parameters used to compare the boundary layers were Re_θ and h/δ.

For the outflow, it was necessary to determine that the results were not dependent on the outflow length. Two simulations were conducted, one with the standard domain and the

other with a longer outflow. The results were compared to determine whether the simulation with the longer outflow yielded different results.

Details of the simulation modeling and grid development will be discussed in the following sections.

3.3.1 Simulation Modeling and Sensitivity Studies

The fluid used for this simulation was air, to match the wind tunnel, and the flow was defined as steady and incompressible. Selecting the correct RANS turbulence model is complex because they are all estimations of the flow and they each have strengths and weaknesses. The suitable turbulence model will vary for different types of flow due to these strengths and weaknesses. To determine the differences between turbulence models and the effect each has on the results, a turbulence model sensitivity study was carried out. In addition to the turbulence model study, a Reynolds number sensitivity study was also conducted. The Reynolds number sensitivity study was based on the tests conducted experimentally in the wind tunnel. Five different Reynolds numbers were examined which corresponded to the wind tunnel free stream velocities of 60 m/s, 50 m/s, 40 m/s, 30 m/s and 20 m/s.

The primary turbulence model investigated in this study was the Spalart-Allmaras model with a curvature correction (SARC). This model selected because it was specifically developed for aerospace applications and has been proven to produce reliable results in wall-bounded flows [11]. For the turbulence model sensitivity study, additional simulations were run using the same grid and Reynolds number, but different turbulence models. The other models investigated were Spalart-Allmaras with no curvature correction (SA) and the $k-\omega$ SST and $k-\epsilon$ two-equation models, both of which have numerous variations available in Star-CCM+.

SARC was set as the "base case" turbulence model for all simulations because it was developed for aerodynamic flows and it is modified from SA to be more accurate for curved geometry. Therefore, it was the turbulence model used for everything except for the turbulence model sensitivity study. SA was also simulated for the turbulence sensitivity study to look at the impact and importance of the curvature correction. An advantage of SA and

SARC is that they are one-equation models, meaning simulations using these turbulence models typically converge faster than the ones that use two-equation models. The simplicity and efficiency of SARC, was another reason SARC was selected as the base case turbulence model.

The other turbulence models used for this study are two-equation models, $k-\omega$ SST and $k-\epsilon$. The $k-\omega$ SST model was chosen because it is known to be able to predict mild separation well and it's often used in aerospace applications because it behaves similarly to SA. Finally, $k-\epsilon$ was selected. This turbulence model tends to predict the separation point further downstream than it actually occurs, or predict no occurrence of separation.

There are many versions of the $k-\omega$ SST and $k-\epsilon$ models in Star-CCM+ and they do not always allow for the same inputs as the simulations that used the SA and SARC models. Specifically, though the low-y^+ wall treatment and the curvature correction were identified as the optimal methods for modeling this flow, and $k-\omega$ SST model did have these two features available, the $k-\epsilon$ model did not. Therefore, three different versions of $k-\epsilon$ were simulated. The first was the lag elliptical model ($k-\epsilon$ LEBM), which had the low-y+ wall treatment and is accurate for near wall modeling in external aerodynamic simulations, but does not have a curvature correction. Then the standard two-layer model was simulated, which uses the all-y+ wall model and does not have a curvature correction available. Finally the realizable two-layer was tested, which does have a curvature correction, but uses the all-y+ wall model [13]. In total, six turbulence models were tested, including SARC.

3.3.2 Grid Generation

The computational grid was generated by an external code, that was developed as a part of this research, and then imported into Star-CCM+. The code used hyperbolic tangent functions and a user-defined number of grid points to generate stretching in the streamwise, spanwise, and vertical directions, independently of each other. The result is a body-fitted, structured mesh that has finer cells near the walls and over the peak of the bump, but stretches to allow for larger cells in regions far from the wall.

Originally the grid stretched in the vertical and streamwise directions but not in the spanwise direction. Initial three-dimensional simulations were conducted with this grid and, although the pressure and skin friction coefficients were aligned with expectations based on two-dimensional simulations and experiments in the wind tunnel, there appeared to be an issue with the simulations that caused the residuals to get hung up on something in the domain.

Two reasons were considered as causes of this issue. The first was that the multigrid solver was limiting the convergence of the simulation. A multigrid solver is a computational technique that speeds up the convergence of the simulation by doing computations on a coarser grid than the one generated for the simulation and using that calculation as an estimate for the actual grid. This is done using a predictor-corrector scheme, by interpolating the fine grid to a coarser grid, computing the result on the coarser grid and then interpolating a correction on that result back down to the finer grid. This method enables the simulations to converge faster, but can sometimes lead to inaccuracies. The other possible issue was that the residuals were getting hung up somewhere in the domain, which would mean that that location would have to be identified and the grid would have to be refined to prevent that hang up.

To investigate whether the multigrid solver was the causing the problems with the residual convergence, a simulation was run where the residuals converged with the solver on and the then the solver was turned off and the simulation ran until the residuals converged again without the multigrid solver. Fig. 3.6 shows the residuals from this simulation. The multigrid solver was turned off around the 13,000-th iteration causing the continuity residual to drop and eventually re-converge. However, the X-, Y- and Z-Momentum residuals remain unaffected, indicating that the multigrid solver was not causing problems in the simulation.

After ruling out the multigrid solver as the issue, a report was run in Star-CCM+ that identified the location of the maximum residuals within the domain. It determined that the maximum value of the X-, Y- and Z-Momentum residuals were all on the sidewalls and the values were significantly lower elsewhere in the domain. Contours of these three residuals

were plotted over the domain, which is shown in Fig. 3.7.

From the contours, it's clear that this spike in residuals occurs in a very localized region on the wall, downstream of the bump. This simulation was run on the original three-dimensional grid, which featured stretching in the vertical and streamwise directions, which was governed by separate hyperbolic tangent functions. Uniform grid spacing was applied in the spanwise direction. It was determined that this uniform spacing was the cause of the residual spike because the first cell off of the side wall was too big to accurately capture the boundary layer. The simulation was therefore unable to resolve the side wall boundary layer, causing the residuals to spike in that region.

To correct this issue, another hyperbolic tangent function was applied in the spanwise direction so that the cells near the wall were much smaller, which enabled them to properly resolve the boundary layers there. The cells in the center of the domain, far from any surfaces, were stretched to be larger than the ones near the wall because the detail in the flow in these regions can be properly resolved with larger cells. The residuals from the simulation with this new grid converged to lower values and the contours did not contain the residual spike on the sidewalls. Therefore the uniform spanwise spacing was determined to be the problem with the original simulation. Fig. 3.8 shows the residual convergence from the two simulations. The X-, Y-, and Z- momentum residual contours were plotted again, shown in Fig. 3.9, which confirms that there is no more residual spike near the wall downstream of the bump.

A list of requirements for the three-dimensional grid were developed: (1) The grid needed to be refined at all walls, including both the sidewalls, and stretched in the center, as described above. (2) The grid spacing in the center could not be larger than it was for the grid with uniform spanwise spacing because it was important not to lose resolution in the far-wall regions. (3) When looking at a spanwise section of the domain, the center cell and the cells at the corner of the domain should be roughly square. This is to ensure an optimal aspect ratio. (4) The ratio between the width or height of one cell to the width or height of the cell before it, which is called the stretching ratio, could not exceed 1.3, with the ideal range being 1.15-1.2.

Through a number of iterations, a grid was developed that met all of these requirements. Spanwise planes upstream of the bump for both the old and new grid are shown in Fig. 3.10.

The wall treatment selected for the simulations was changed from the all-$y+$ model to the low-$y+$ treatment. The all-$y+$ model is the default in Star-CCM+, but this model is used to speed up the simulation time by modeling the near-wall behavior rather than directly solving for it, which is what the low-$y+$ wall treatment does. The all-$y+$ treatment is recommended for simulations where the first $y+$ point is in the log-law layer of the boundary layer, meaning it is roughly $y+ = 30$, or greater. The low-$y+$ treatment is used for simulations with a grid that has $y+ = 5$, or less, as the first point. Therefore, the low-$y+$ wall treatment resolves the viscous sublayer with little or no modeling [13]. This wall treatment has a much higher computational expense, but because the intent of these simulations is to test the RANS turbulence models, it is important that there are no other models being tested. Thus, switching from the all-$y+$ wall model to the low-$y+$ wall is critical for this research.

The pressure and skin friction coefficients computed by the updated simulation were compared to the old simulation and the plots of the streamwise and spanwise centerlines results are shown in Fig. 3.11 and Fig. 3.12, respectively.

The most significant change between these two datasets is the skin friction coefficient along the streamwise centerline. This is likely a result of switching from the all-$y+$ wall model to the low-$y+$ wall treatment. There is also a noticeable change in the spanwise pressure coefficient at the side walls, likely a result of using the stretched grid with refinement at the sidewalls.

3.3.3 Boundary Conditions and Inflow and Outflow Lengths

A study was conducted to determine whether the simulation results were sensitive to the downstream length of the domain. Two grids were developed in two-dimensions. The first grid was the standard domain, which was symmetrical around the peak of the bump. Upstream of the bump there was $1L$ of slip wall, followed by $1L$ of no-slip wall. In the second half of the domain, downstream of the bump, the entire $2L$ is a no-slip wall. The second grid

developed was the same as the first but the downstream length of the domain was increased from $2L$ to $3L$. The simulations were conducted at the highest Reynolds number in the testing range, 3.41×10^6, using the SARC turbulence model and all inputs to the simulations were identical except for the downstream lengths of the domains.

The pressure and skin friction coefficients from the two simulations, which are shown in Fig. 3.13, indicate that the results are not sensitive to the downstream length because the data from the two simulations overlap completely.

The grid is generated outside of Star-CCM+ and then imported into the simulations is one single element. Therefore, in order to assign the boundary conditions, the rectangular domain must be split into six different faces. Then the top, bottom and sidewalls of the domain each have to be split into two faces so that the first $1L$ of each face can be designated as a slip wall and the remainder is a no-slip wall. While iterating and improving the simulations, it became clear that the domain was not be split at the correct location during the early simulations, this led to a slip wall that was shorter than $1L$ and a no-slip boundary layer development length that was longer than $1L$. As a result, at $-0.65L$ ahead of the peak of the bump, the simulation boundary layer was thicker than the experimental boundary layer and the two did not match. Once this problem was identified, it was corrected by creating a function in Star-CCM+ that split the faces of the domain at a specified location. Simulations conducted following this correction showed that the simulation and experimental boundary layers matched at $-0.65L$ ahead of the peak of the bump, confirming that $1L$ was the correct inflow length.

Fig. 3.14 shows a plot of Re_x vs. Re_θ for all the different turbulence models simulations. These are compared to the NASA zero pressure gradient standard result. Note, the vertical black line in both plots indicates the boundary layer measurement location from experiments and simulations, $0.65L$ ahead of the peak of the bump.

Initially, only the SARC incoming boundary layer was compared to the NASA result and it was clear that the two, though not perfectly matched, were similar. Now it is clear that there is a much larger discrepancy between the NASA boundary layer and the incoming

boundary layers produced by some of the other turbulence models. The $k-\epsilon$ models in particular do a poor job matching the inflow. However, $k-\omega$ SST follows the NASA profile well.

Fig. 3.14 also shows plots of the boundary layer thicknesses upstream of the bump for the different turbulence models. The inflow length was originally decided using SARC simulation results and from Fig. 3.14, it is clear that at the boundary layer measurement location (indicated by the vertical black line) the boundary layer thickness predicted by the turbulence models falls into two groups: SARC, SA and $k-\epsilon$ Standard Two-Layer predict a thicker boundary layer than $k-\omega$ SST, Realizable $k-\epsilon$ and $k-\epsilon$ LEBM. The inflow length of $1L$ was determined based on the SARC inflow, but this boundary layer thickness plot suggests that, if the inflow was determined using $k-\omega$ SST, the inflow length might have to be increased because the boundary layer for $k-\omega$ SST is much thinner at $x/L = -0.65$ than the SARC boundary layer.

3.3.4 Grid Convergence Study

After confirming the inflow and outflow lengths, a grid convergence study was conducted to select the ideal three-dimensional grid for future simulations. All three grids used had to follow the grid parameters identified previously, which were: (1) grid was refined at all walls and stretched in the center, (2) spacing in the center still had enough resolution to capture the detail of the flow, (3) cells were roughly square at the center and the corners of the domain, and (4) stretching ratio did not exceed 1.3, with the ideal range being $1.15-1.2$.

A coarse, medium and fine grid were generated and the simulations for the different grids were conducted at 60 m/s using SARC. All Star-CCM+ simulations were run on Hyak, a supercomputer used for research at UW, which cut the simulation time for three-dimensional simulations down from a week or more when run on a desktop computer, to anywhere from a couple hours to 12 hours, depending on the grid resolution. This was a huge advancement that allowed for finer grids and more simulations to be run.

The coarse, medium and fine grids were $260\times250\times120$, $338\times312\times150$, and $364\times334\times160$,

respectively. The stretching ratios in the vertical direction were determined to be 1.17, 1.17, and 1.16 for the coarse, medium and fine grids and the spanwise stretching ratios were 1.08, 1.088, 1.078. Therefore these grids satisfied the stretching ratio parameter.

Plots of the pressure and skin friction coefficients are shown in Fig. 3.15. While the results from the coarse grid deviate slightly, the results from the medium and fine grids overlap. Table 3.1 details all the significant parameters from the grid convergence simulations. The medium and fine grids have very similar values of h/δ and Re_θ, another indication that the results have converged.

The grid convergence index (GCI), developed by Roache [27] was used to determine the level of convergence. This calculation was done following the procedure outlined by Celik et al. [28]. First, the grid size, h is calculated for each grid using the equation 3.1.

$$h = \left[\frac{1}{N} \sum_{i=1}^{N} (\Delta A_i) \right]^{(} 1/2) \tag{3.1}$$

The area of the ith cell is (ΔA_i) and N is the total number of cells in the grid. The next step is to calculate the grid convergence factor, r, which is a ratio between the grid sizes of the coarse and fine grids, h_{coarse}/h_{fine}. The next step is to calculate the approximate relative error, shown in equation 3.2.

$$e_a = \left| \frac{\phi_1 - \phi_2}{\phi_1} \right| \tag{3.2}$$

The GCI can be determined using any flow property, ϕ. The flow property corresponding to the fine grid is ϕ_1 and ϕ_2 is the flow property corresponding to the medium grid. The relative error calculation can also be calculated between the medium and coarse grid, using flow properties corresponding to those grids. The apparent order p, must be calculated using equation 3.3.

$$p = \frac{1}{\ln(r_{21})} \left| \ln \left| \frac{\epsilon_{32}}{\epsilon_{21}} \right| + q(p) \right| \tag{3.3}$$

Where $\epsilon_{32} = \phi_3 - \phi_2$ and $\epsilon_{21} = \phi_2 - \phi_1$. The following equations can be used to calculate q and s

$$q(p) = \ln\left(\frac{r_{21}^p - s}{r_{32}^p - s}\right) \tag{3.4}$$

$$s = sgn\left(\frac{\epsilon_{32}}{\epsilon_{21}}\right) \tag{3.5}$$

The final step is to calculate the GCI for the medium and fine grids and also for the coarse and medium grids. The equation for the medium and fine grids is shown in equation 3.6.

$$GCI_{fine}^{21} = \frac{1.25e_a^{21}}{r_{21}^p - 1} \tag{3.6}$$

The grid convergence index was calculated at the bump peak for the skin friction and pressure coefficients between the coarse and medium grids and between the medium and fine grids. The results are shown in Table 3.2. Thus, the medium grid was selected as the standard grid used for subsequent simulations because it produced nearly the same results as the fine grid, but it required less computation time to simulate.

Grids	GCI_{C_f}	GCI_{C_f}
Coarse to Medium	0.0842%	0.0339%
Medium to Fine	0.0029%	0.0025%

Table 3.2: Grid convergence index for skin friction and pressure coefficients for the three grids examined in the grid convergence study.

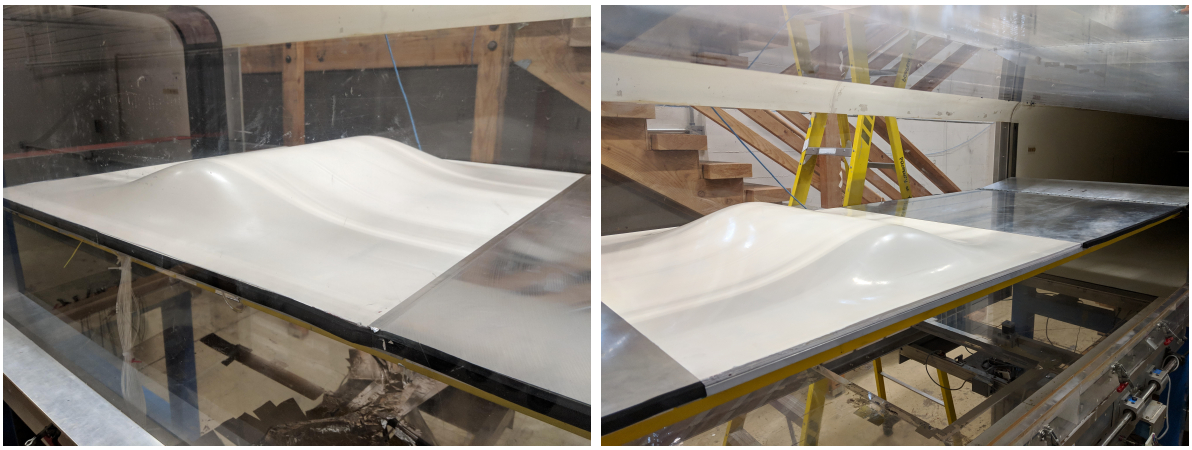

(a) (b)

Figure 3.4: Three-dimensional bump mounted on splitter plate and installed in the wind tunnel test section. (a) Looking upstream (b) Looking downstream.

Grid Size	$Re_L(x10^{-6})$	z^+_{min} in BL	z^+_{min} on bump	y^+_{min} on wall	$Re_\theta(x10^{-3})$	h/δ
$260 \times 250 \times 120$	3.41	0.613	3.085	0.622	2.60	11.72
$338 \times 312 \times 150$	3.41	0.062	0.454	0.099	2.59	11.87
$364 \times 334 \times 160$	3.41	0.038	0.302	0.092	2.58	11.77

Table 3.1: Significant parameters from the grid comparison simulations. The z^+_{min} in the boundary layer, Re_θ, and h/δ were all measured at $0.65L$ ahead of the peak of the bump, which is the same location as all of the boundary layer measurements in the experiments.

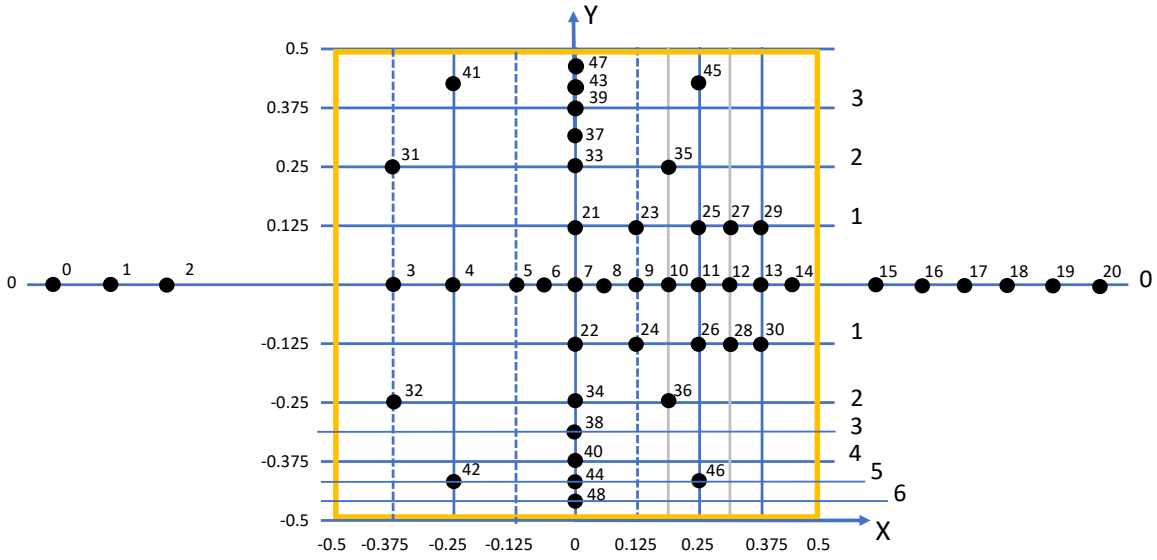

Figure 3.5: Location of pressure taps on the bump and splitter plate as shown from above. Upstream is to the left and the flow moves to the right. Distances normalized by L_b.

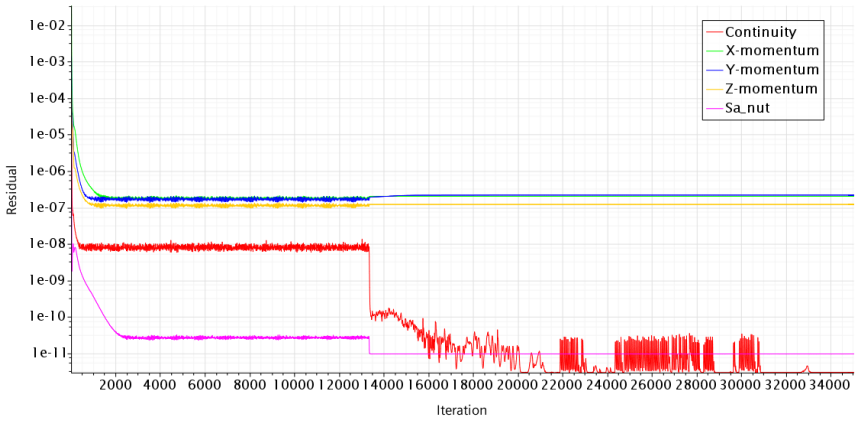

Figure 3.6: Residuals from simulation with multigrid solver turned off.

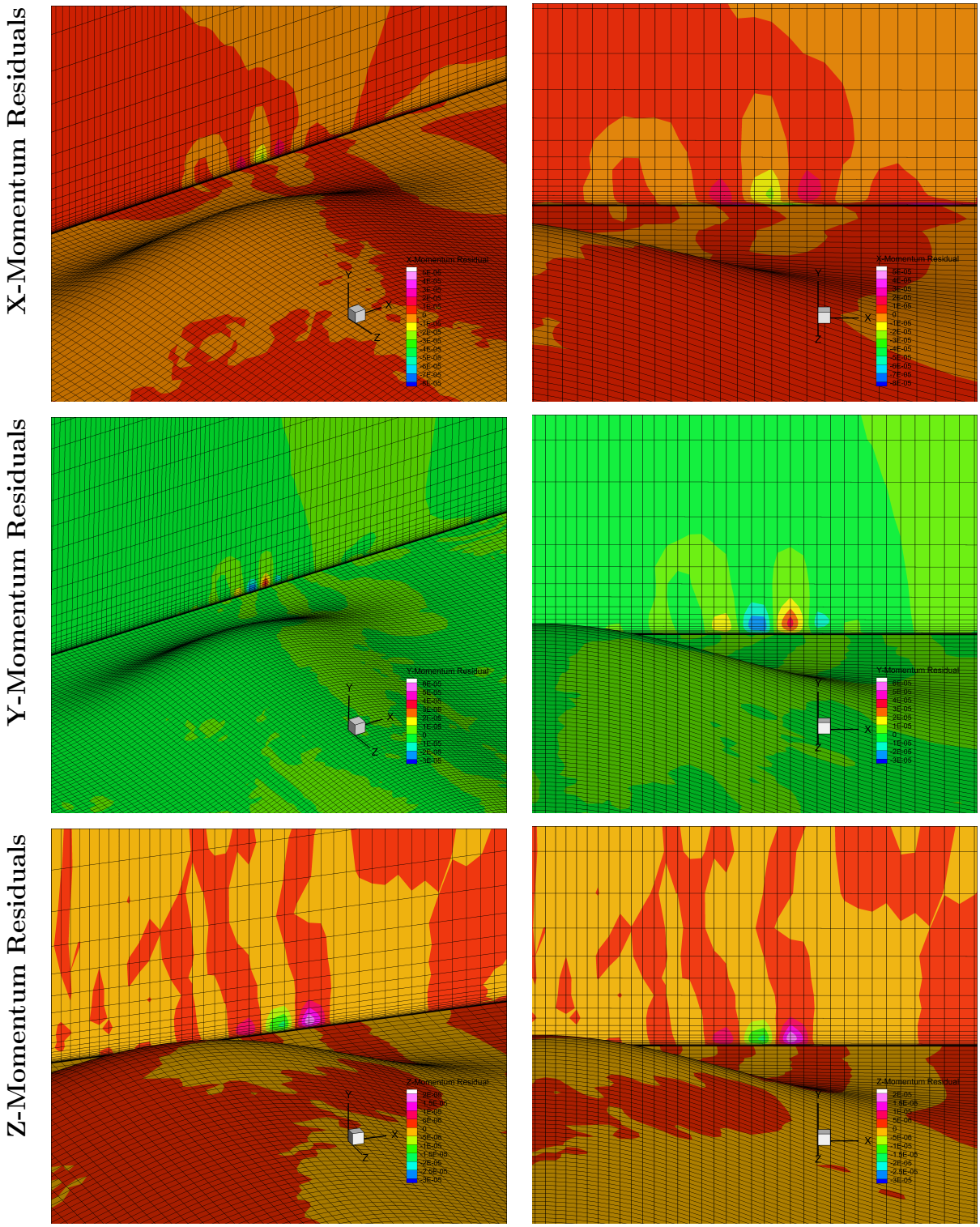

Figure 3.7: X-, Y-, and Z-Momentum residuals for grid with uniform spacing in the spanwise direction.

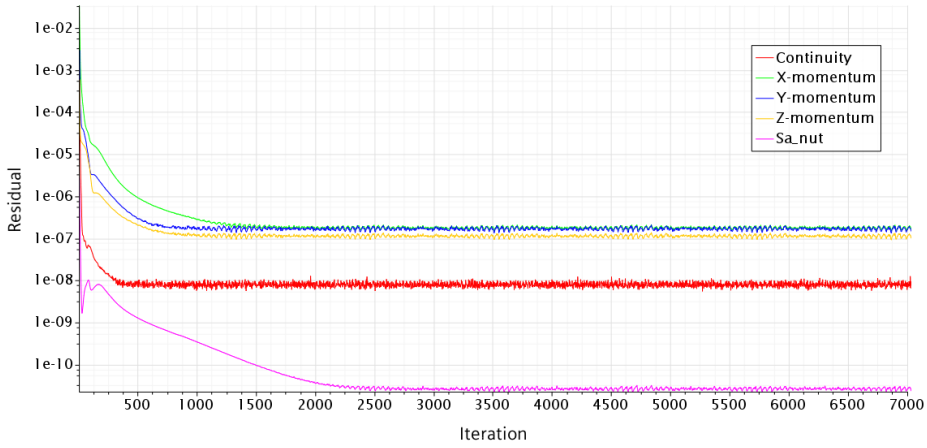

(a)

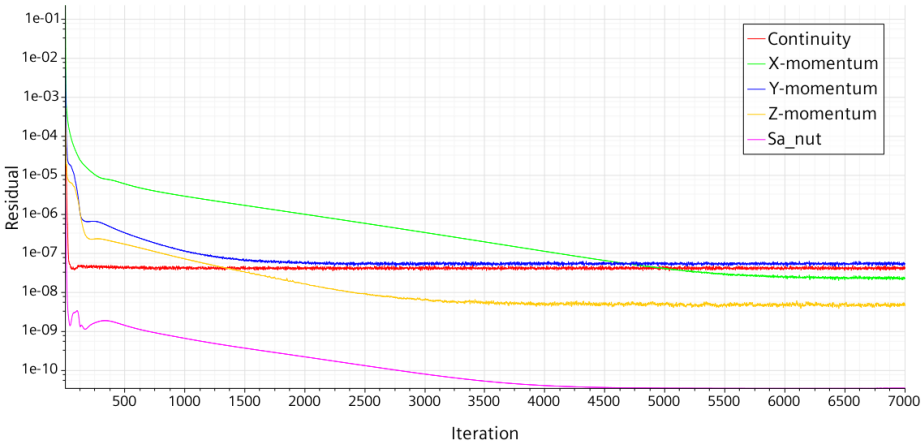

(b)

Figure 3.8: Residual convergence for (a) original 3D grid with uniform spanwise spacing and (b) refined grid with grid stretching toward the side walls.

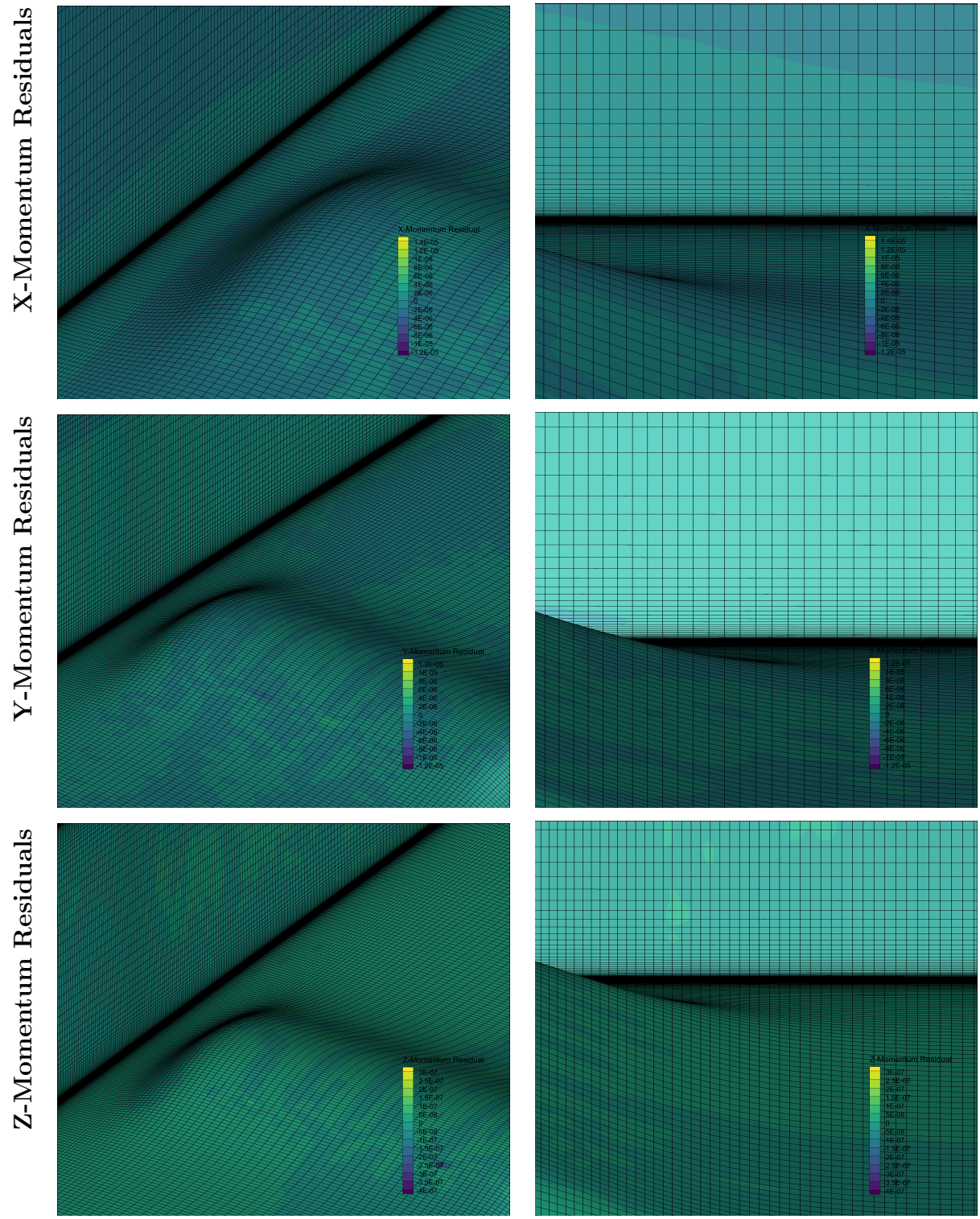

Figure 3.9: X-, Y-, and Z-Momentum residuals for grid with stretching in the spanwise direction.

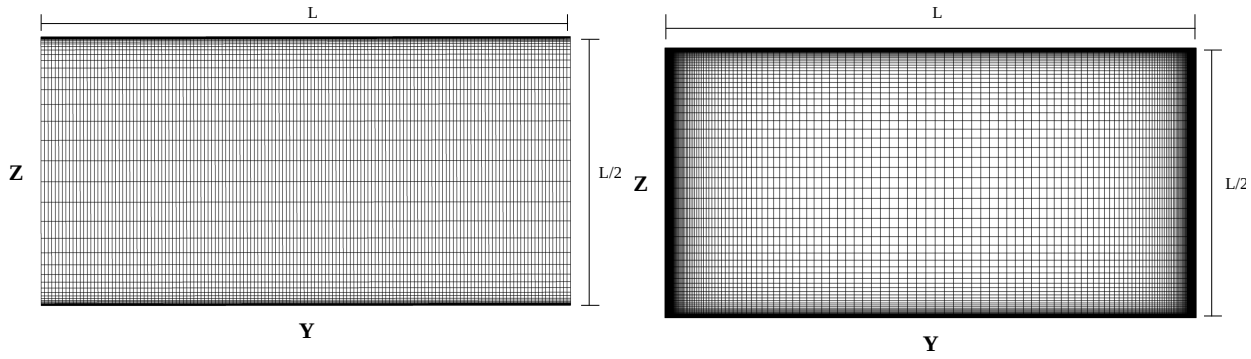

(a) (b)

Figure 3.10: Spanwise/wall-normal grids upstream of the bump. (a) Old configuration (b) new configuration.

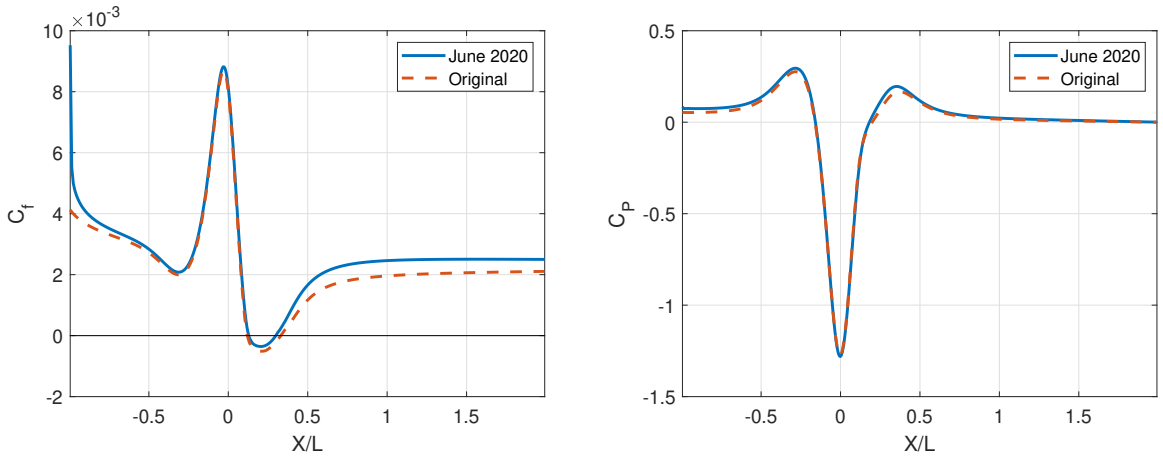

(a) (b)

Figure 3.11: Comparison of (a) skin friction and (b) surface pressure profiles for grid with uniform spanwise spacing (Original) and stretching in the spanwise direction (June 2020) along streamwise centerline.

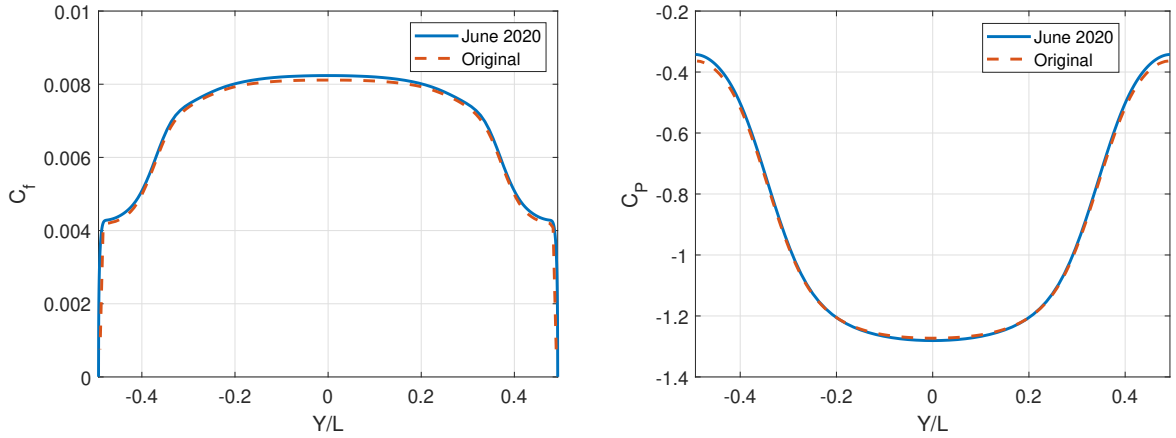

(a) (b)

Figure 3.12: Comparison of (a) skin friction and (b) surface pressure profiles for grid with uniform spanwise spacing (Original) and stretching in the spanwise direction (June 2020) along spanwise centerline.

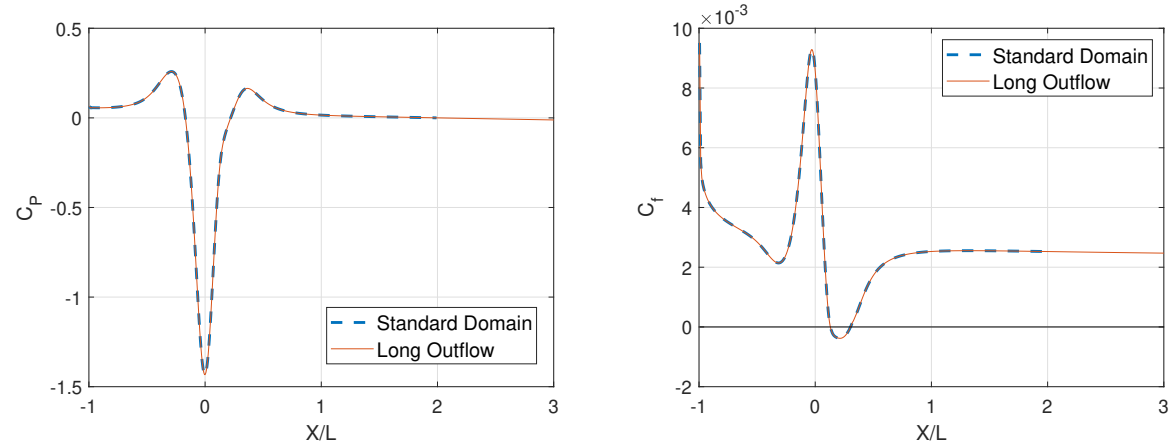

(a) (b)

Figure 3.13: Comparison between the pressure and skin friction coefficients determined by the two dimensional simulations with differing outflow lengths.

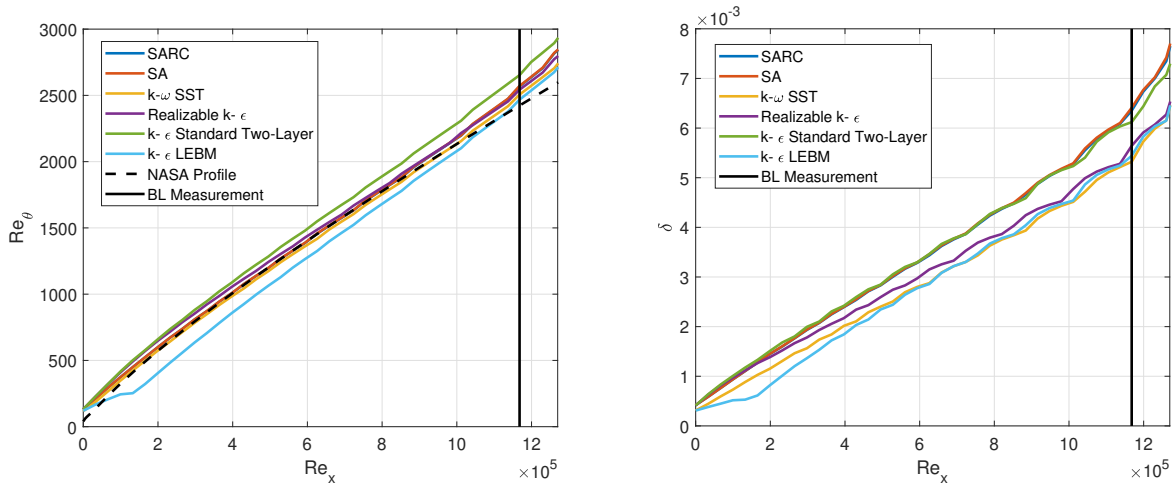

(a) (b)

Figure 3.14: (a) Comparison of simulated boundary layer upstream of the bump to NASA zero pressure gradient standard result. Comparison includes numerous turbulence models. Conditions at $x/L = -0.65$ correspond very closely to experimental results. (b) Simulated boundary layer thickness upstream of the bump determined by numerous turbulence models.

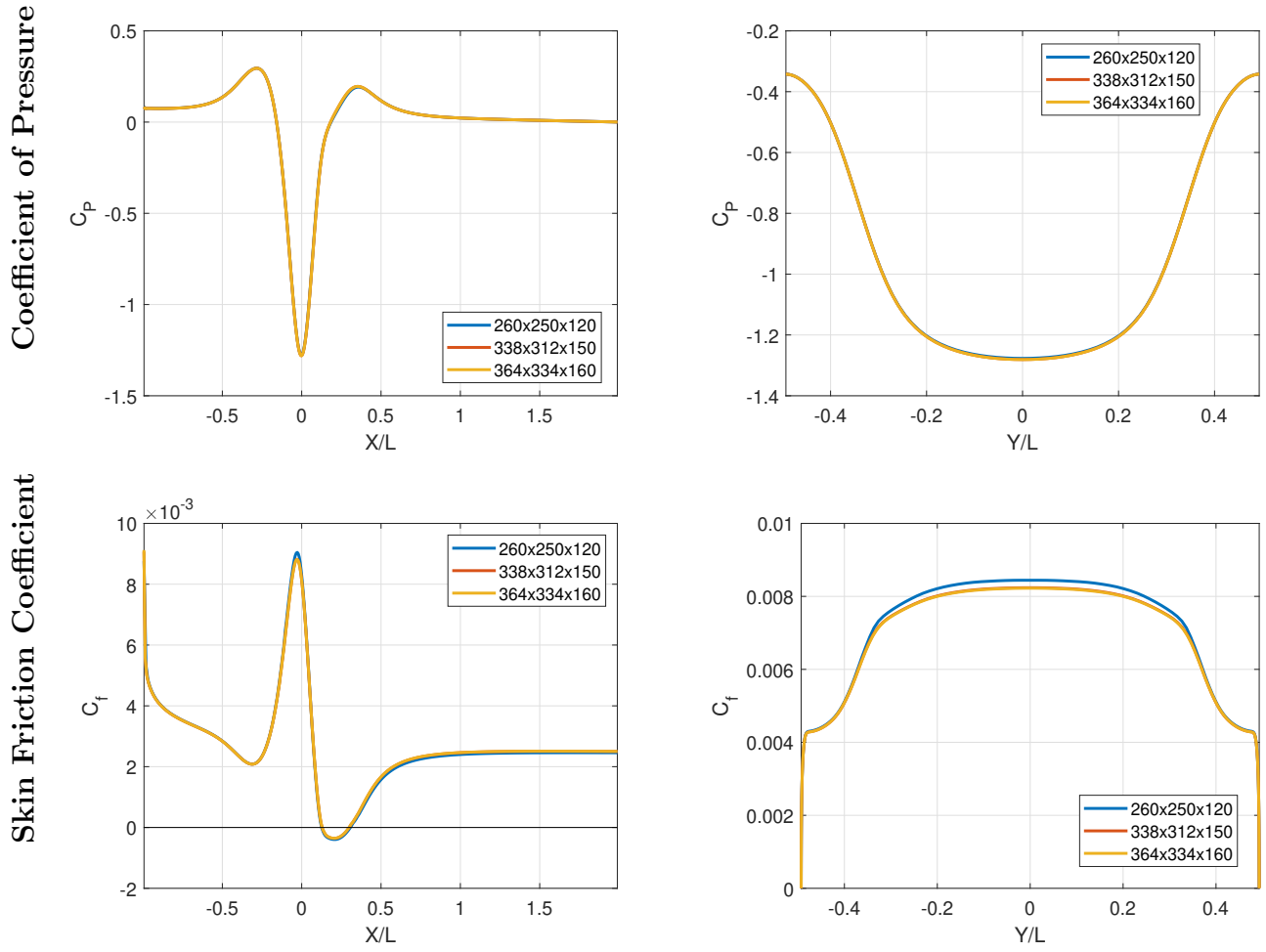

Figure 3.15: Pressure and skin friction coefficients along the streamwise and spanwise centerlines comparing the three grids examined. It was determined that the medium grid, $338 \times 312 \times 150$, was the ideal grid for the simulations.

Chapter 4

RESULTS AND DISCUSSION

Experimental boundary layer measurements and surface pressure data were collected at four different locations in the wind tunnel, corresponding to four different levels of vertical confinement. Station 4 was the centerline location, with H/L = 1/2. The subsequent locations all had more confinement: station 3 (H/L = 5/12), station 2 (H/L = 1/3) and station 1 (H/L = 1/4). Experimental and computational incoming boundary layers were compared to ensure their similarity. The experimental surface pressure data was used to investigate the effect of Reynolds number and confinement on the bump flowfield and to provide an initial validation dataset for the simulations. Corresponding simulations were only conducted at the centerline location, station 4. These simulations were used to examine the effect of Reynolds number on the simulation flowfield and the effectiveness of some of the most common RANS models in accurately predicting the flow. Surface visualizations from the simulations were used to identify primary flow structures and to compare to experimental surface flow visualizations.

4.1 Boundary Layer Measurement

A mechanical traverse was used to measure the boundary layer profile, upstream of the bump at X/L = −0.65. The boundary layers were measured to confirm that the incoming boundary layers in the experiments and simulations corresponded closely and to confirm that the incoming boundary layer was fully turbulent for each velocity tested. These tests were carried out originally by Sage Sarwas and discussed in their thesis [25] and then continued for the research related to this thesis. Since the completion of that thesis, the three-dimensional simulations have been completed. This data was subsequently analyzed to determine an

appropriate inflow length for three-dimensional simulations such that the BL thickness closely matched the experiments.

Table 4.1 shows some important simulation parameters from the Reynolds sensitivity study. The first column lists the Reynolds number based on the bump width, Re_L, which, starting with the first row, correspond to freestream velocities of 60 m/s, 50 m/s, 40 m/s, 30 m/s and 20 m/s. The table also includes the z^+_{min} at the boundary layer measurement location, $X/L = -0.65L$, and on the peak of the bump, and y^+_{min} on the sidewall, which is constant throughout the domain. The last two columns are values from the boundary layer measurement location, the Reynolds number based on the momentum thickness, Re_θ, and the normalized boundary layer thickness, h/δ. The results for both the simulations and the experiments are included. The simulations and experiments have similar values for the two highest Reynolds number cases, $Re_\theta = 2.59 \times 10^3$ and $Re_\theta = 2.64 \times 10^3$ for the simulations and experiments, respectively. The boundary layer thicknesses are also similar, $h/\delta = 11.87$ for the simulation and $h/\delta = 12.0$ for the experiments. The agreement in these values is also seen in the two lowest Reynolds number cases, which are also displayed in this table. This agreement between the values indicates that the incoming boundary layers match sufficiently for comparison.

Fig. 4.1 shows the boundary layer profile at $-0.65L$ ahead of the peak of the bump for the SARC turbulence model, plotted alongside the experimental boundary layer measured in the wind tunnel at the same location for three different velocities: 60 m/s, 30 m/s and 20 m/s. This data was taken at the vertical position of $H/L = 1/2$. All profiles exhibit the characteristics structure of the log-law profile for a turbulent boundary layer. The viscous sublayer is not discernible in the experimental data as it is too close to the surface to measure accurately. However, the log and wake regions are visible in both data sets so comparisons can be made between experiments and simulations in the logarithmic and wake portions of the profiles. It is clear from the experimental data that all the experimental boundary layers are well-tripped and developed. The wake size of the boundary layer profiles was analyzed and discussed in previous work related to this project, which was also used to conclude that

the boundary layers are turbulent and well-developed [26, 25].

The simulation and experimental profiles for 60 m/s and 30 m/s overlap well, but the comparison at 20 m/s is less good. As Reynolds numbers get lower, there are more remnants of the transition from laminar to turbulent boundary layer in the experiments. Influence of the transition process on outer layer curvature of the mean profile is greater, but the model does not simulate the transitional or laminar region at all, which is why the lowest Reynolds number case (freestream velocity of 20 m/s) shows the greatest difference between experiments and simulations. For this reason, the 20 m/s case should be considered with greater caution. It is possible that the 20m/s case is relaminarizing on the upstream slope of the bump, which is a further cause for concern. This possibility will be investigated in an upcoming particle image velocimetry (PIV) experiments.

The boundary layers at 60 m/s, 30 m/s and 20 m/s were also plotted for the different levels of confinement. Fig. 4.2, 4.3 and 4.4 shows the plots at station 3 (H/L = 5/12), station 2 (H/L = 1/3), and station 1 (H/L = 1/4). These plots demonstrate that the turbulent boundary layers are well-tripped and well-developed for all levels of vertical confinement that were tested.

4.2 Surface Pressure

The following analysis of surface pressure results will be divided into two main sections. One will focus on the data collected at station 4, which is the centerline location in the tunnel. This will include a discussion of the sensitivity of the flow to Reynolds number variations, which was conducted at this position both experimentally and computationally. This section will also discuss the RANS turbulence model sensitivity study that was conducted at this location. The subsequent section will focus on the influence of flow confinement on surface pressure profiles. Four plate locations were examined, over the same range of Reynolds numbers.

	Re_L ($\times 10^{-6}$)	BL z^+_{min}	Peak z^+_{min}	Sidewall y^+_{min}	$Re_\theta (x10^{-3})$	h/δ
Sims.	3.41	0.0622	0.4544	0.099	2.59	11.87
	3.04	0.0559	0.4078	0.0891	2.35	11.62
	2.46	0.046	0.3338	0.0733	1.96	11.28
	1.87	0.0358	0.2561	0.0569	1.55	10.98
	1.32	0.026	0.1827	0.0414	1.15	10.58
Exps.	3.41	-	-	-	2.64	12.0
	1.87	-	-	-	1.56	10.8
	1.32	-	-	-	1.16	10.1

Table 4.1: Flow and simulation characteristics for the Reynolds number sensitivity simulations and experiments at the vertical position $H/L = 1/2$. The grid used in all of these cases was the medium grid with $338 \times 312 \times 150$ grid points.

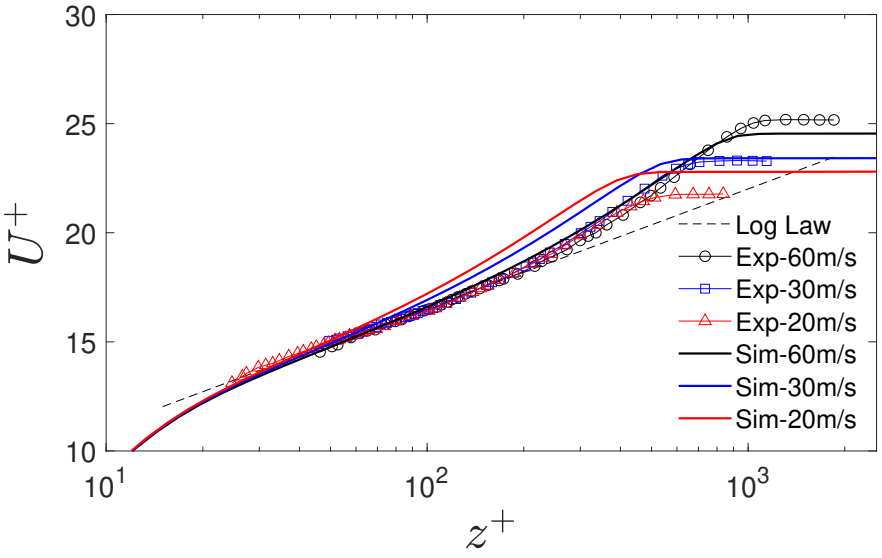

Figure 4.1: Simulated boundary layer profile at x/L = -0.65 for 60 m/s, 30 m/s and 20 m/s, compared to the experimental boundary layer measured at the same velocities.

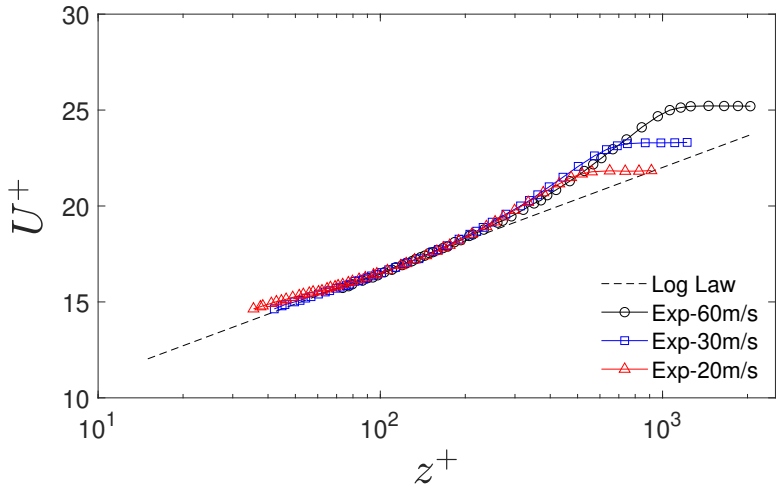

Figure 4.2: Experimental boundary layer profiles at station 3 (H/L = 5/12) and at x/L = -0.65 for 60 m/s, 30 m/s and 20 m/s.

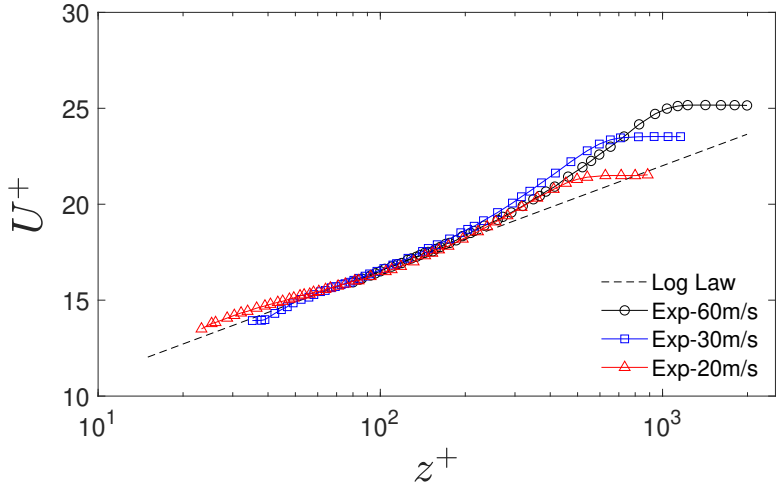

Figure 4.3: Experimental boundary layer profiles at position 2 (H/L = 1/3) and x/L = -0.65 for 60 m/s, 30 m/s and 20 m/s.

4.2.1 Plate at tunnel centerline ($H/L = 1/2$, Station 4)

Sensitivity of Gaussian bump flowfield to Reynolds number variations

Experimental surface pressure data collected from the full range of Reynolds numbers is shown in Fig. 4.5. This data is from the vertical position of $H/L = 1/2$. All pressure taps measurements are included. The reference pressure was taken at Tap 0 for all experiments and simulations. The first twenty taps correspond to the centerline of the tunnel, with subsequent taps in spanwise-symmetric pairs on the bump. The flow is roughly symmetric across the streamwise centerline, with pairs of corresponding taps being either equal, or close to each other in value. However, there is some asymmetry between tap pairs, particularly in the separated region, but no bias to either side of the bump is present. This asymmetry is also evident in Fig. 4.8, which shows the pressure coefficients across the spanwise centerline. The second tap out from the centerline on either side should be the same or similar, based on the symmetry of the geometry, but the one on the positive side (around $Y/L = 0.25$) in much more negative than the tap on the negative side (around $Y/L = -0.25$). At this time, the asymmetry is assumed to be an experimental issue, as it was not present in any simulations. Tests will be conducted to determine the wind tunnel's inflow uniformity by Master's student Matt Robbins, which should help determine the cause of the asymmetry.

These results are compared to the simulation results for the same Reynolds numbers and the same level of confinement ($H/L = 1/2$) in Fig. 4.6, which shows the streamwise centerline, Fig. 4.7, which highlights the separated region along the streamwise centerline, and Fig. 4.8, which shows the spanwise centerline. The SARC turbulence model was used for all simulations in this case. Error bars are present on these pressure coefficient measurements, determined through an uncertainty analysis conducted by Master's student Matt Robbins and discussed in a paper, which will be presented at SciTech 2021 [29].

The streamwise centerline results show that, while there is agreement between the experimental and computational profiles in the attached regions, the results do not agree in the separated region. The experimental data in the separated region shows an inflection point

around $X/L = 0.1$ in all velocity cases. While this inflection point is observed in the lower Reynolds number cases in the simulations (freestream velocity of 20 m/s and 30 m/s), it disappears from the three higher Reynolds number cases. The experiments and simulations both suggest that the flow is Reynolds number insensitive at $Re_L = 2.46 \times 10^6$ and above.

The simulation results show an opposite Reynolds number trend to the experimental results. Fig. 4.7 shows that, in the experiments, upstream of $X/L = 0.1$ the high velocity has a smaller pressure magnitude than the lower velocity cases, and after the inflection point (downstream of $X/L = 0.1$) the high velocity case has a greater pressure coefficient magnitude. In the RANS simulations, the low velocity case has the lesser magnitude upstream of $X/L = 0.1$ and and the greater magnitude downstream of $X/L = 0.1$. Another instance of this opposite trend can be seen in Fig. 4.6 and 4.8. In the experiments, the pressure coefficient at the top dead center of the bump has the largest magnitude for the 20 m/s case. However in the simulations, the 60 m/s case is the one that leads to the largest pressure coefficient magnitude at this location. The spanwise centerline in Fig. 4.8 also shows that, in the experiments, the profile over the top of the bump has a two peaks, where the two taps on either side of the center tap have a more negative pressure coefficient than the center tap, and this trend was observed in all experimental velocities except for the 20 m/s case. While this shape is observed in the simulation data for the 20 m/s case, in all the higher velocity cases, the pressure coefficient reaches it's minimum value at the center and there is no double peaked profile.

The skin friction coefficient was not measured experimentally, but the skin friction coefficients from the simulations are shown in Fig. 4.9 and 4.10, which shows the streamwise and spanwise centerlines centerline at all Reynolds numbers. The skin friction coefficient along the streamwise centerline demonstrates that the flow separates for all velocities tested, observed when the value of skin friction is zero or negative. The three high Reynolds number cases (60 m/s, 50 m/s, and 40 m/s) appear to separate at a very similar point, while the two lower cases separate slightly farther upstream. The lowest Reynolds number case, corresponding to 20 m/s, separates first. There is a more significant difference between

where the flows reattach, with the higher Reynolds number cases reattaching first, all at similar locations, followed by the lower Reynolds number cases further downstream. Therefore, the simulations predict that the results become insensitive to the Reynolds number for $Re_L = 2.46 \times 10^6$ and greater, but the separation and reattachment depend on the Reynolds number below $Re_L = 2.46 \times 10^6$. The two lowest velocity cases appear to reattach at about the same location. Therefore, from this study it's concluded that SARC predicts that the low Reynolds number cases have a larger separated region than the high Reynolds number cases because the higher Reynolds number cases separate downstream of the low ones and reattach upstream of them.

The streamwise centerline plot also shows that the 60 m/s, 50 m/s and 40 m/s cases all have similar skin friction profiles in the outflow, which is the region at the end of the domain where the flow is reattached, around $X/L = 0.5$ to the end of the domain. The 30 m/s and 20 m/s are different from the higher velocity cases and from each other. This is more evidence of the insensitivity to Reynolds number discussed previously. This sensitivity below a certain Reynolds number could indicate that the there is a phenomena occurring in the real flow that the simulations cannot capture. The skin friction coefficient along the spanwise centerline shown in Fig. 4.10 shows that the Reynolds numbers have a strong effect on the skin friction coefficient across the span of the bump and close to the wall. The two highest Re_L cases have similar profiles and similar maximum values and the middle profile has a similar shape to them, but the two lowest Re_L cases are different from the rest of the cases and each other.

Turbulence Model Sensitivity Study

A series of RANS simulations were conducted with a range of common models at $Re_L = 3.41 \times 10^6$, which corresponds to a freestream velocity of 60 m/s. These tests highlighted the importance of the curvature correction and displayed widely ranging behaviors in the separated region. The turbulence models tested were Spalart-Allmaras with a curvature correction (SARC), which was used for all the simulations in the Reynolds number sensitivity

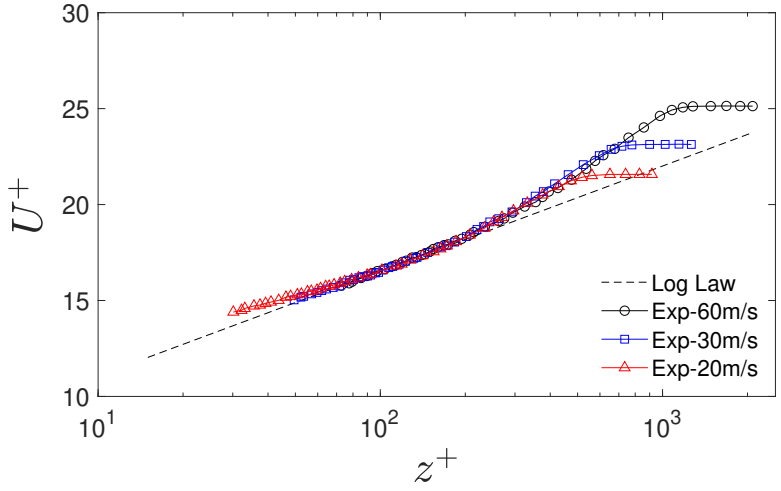

Figure 4.4: Experimental boundary layer profiles at position 1 (H/L = 1/4) and x/L = -0.65 for 60 m/s, 30 m/s and 20 m/s. This was the case with the most vertical confinement.

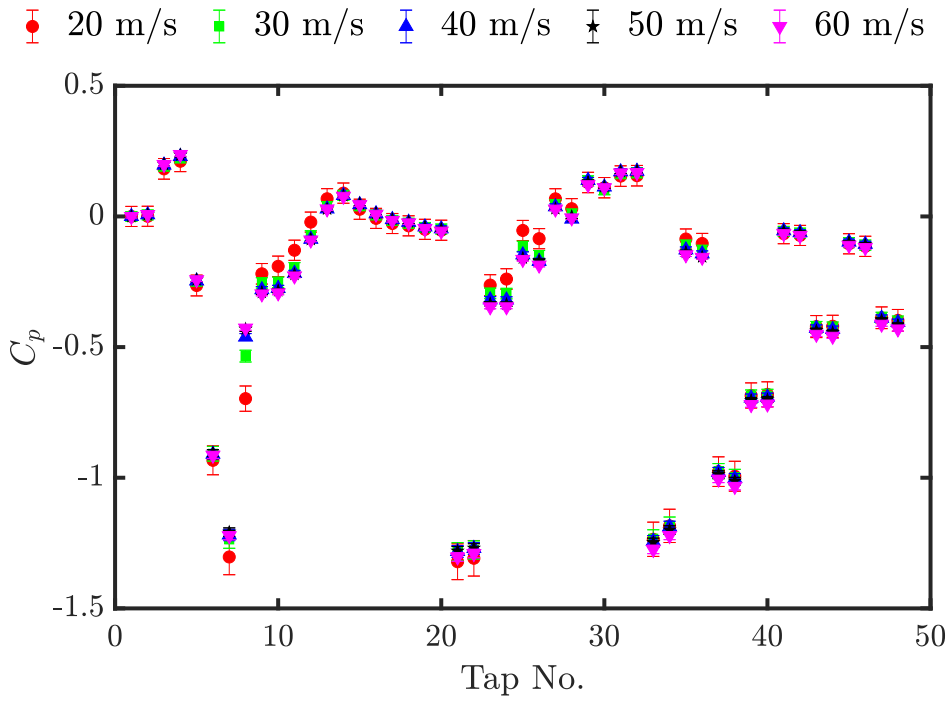

Figure 4.5: Survey of all experimental pressure coefficient data for vertical position H/L = 1/2. Tap numbers correspond to locations in Figure 3.5.

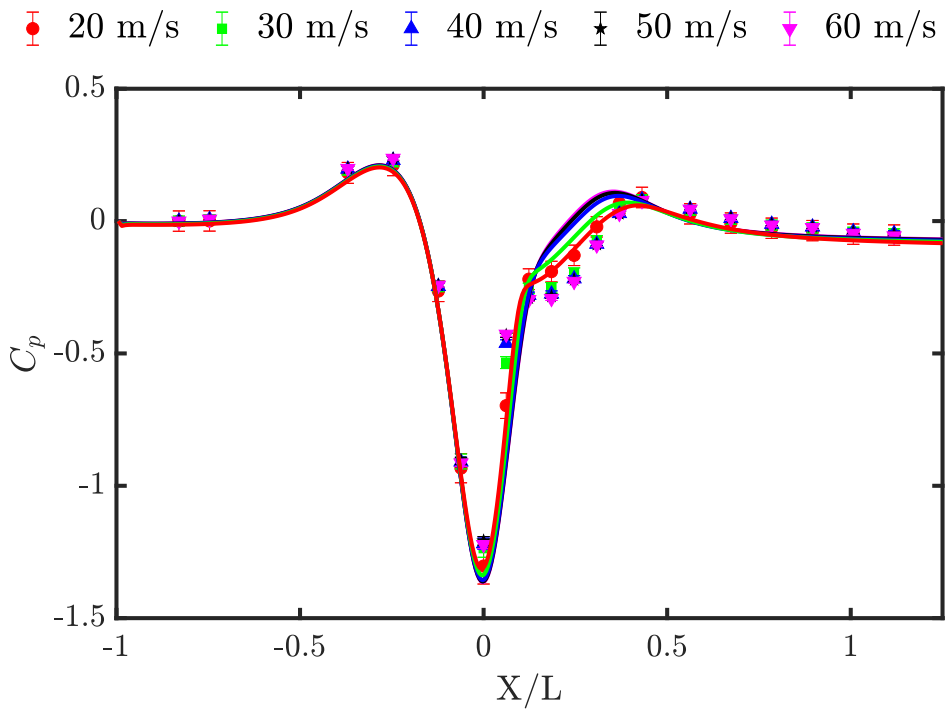

Figure 4.6: Variation in pressure along the streamwise centerline for experimental and simulation data at the vertical position $H/L = 1/2$. Solid lines and points correspond to simulation and experimental data, respectively. Simulations used SARC.

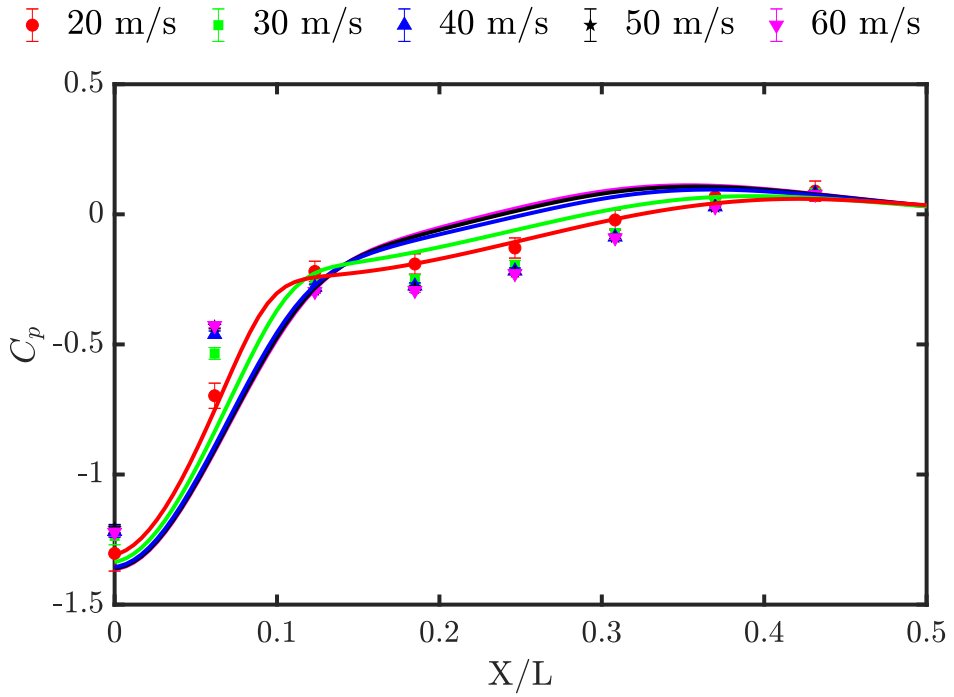

Figure 4.7: Highlighting the separated region shown in Fig. 4.6. Vertical position $H/L = 1/2$ and simulations used SARC.

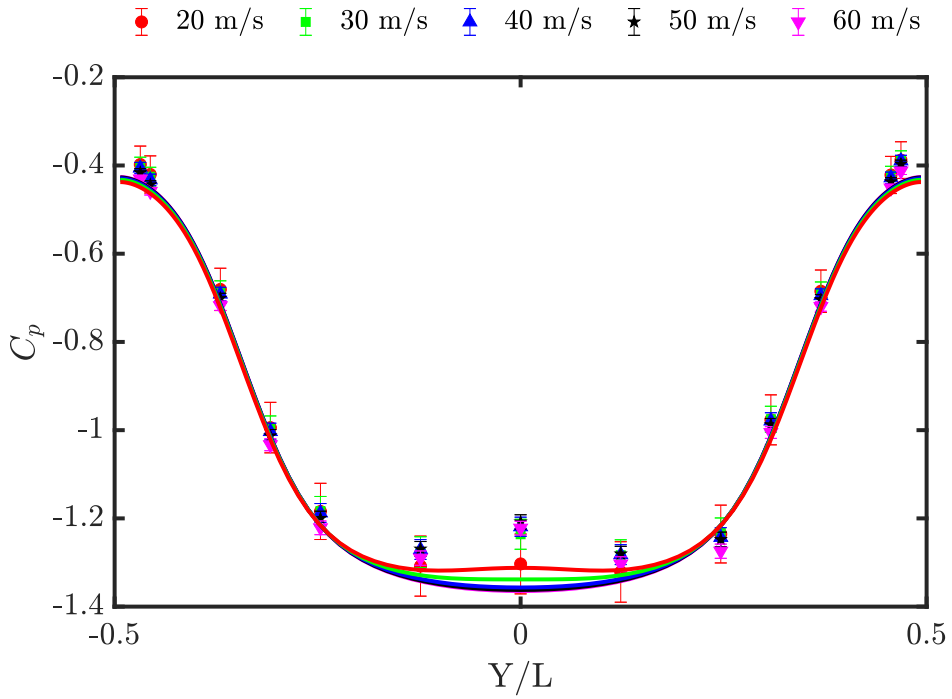

Figure 4.8: Variation in pressure along the ridge of the bump ($x = 0$). Cases as in Figure 4.6. Vertical position $H/L = 1/2$ and simulations used SARC.

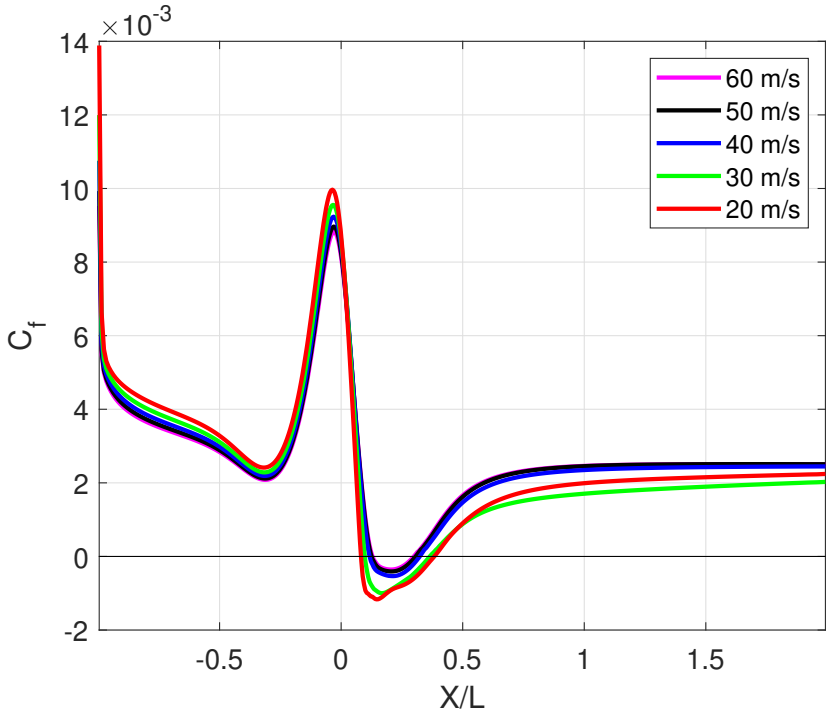

Figure 4.9: Variation in skin friction coefficient along the streamwise centerline. Cases as in Figure 4.6. Vertical position $H/L = 1/2$ and simulations used SARC.

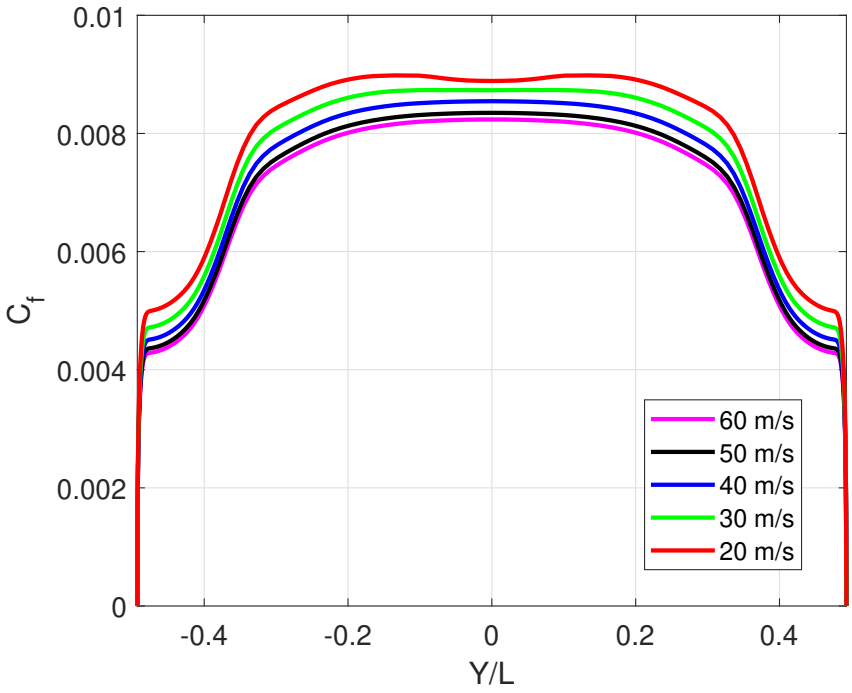

Figure 4.10: Skin friction coefficient along along the ridge of the bump ($x = 0$). Cases as in Figure 4.6. Vertical position $H/L = 1/2$ and simulations used SARC.

study, standard Spalart-Allmaras (SA), $k-\omega$ SST with a curvature correction, and three versions of $k-\epsilon$: lag elliptic blending model (1), standard two-layer (2) and realizable two-layer (3). The difference between the three $k-\epsilon$ models were discussed in Chapter 3.

Table 4.2 displays the important grid and flow parameters for each turbulence model. The six turbulence models are compared to each other and the experimental result at the same Reynolds number. SARC and $k-\omega$ SST display very different values of h/δ at $X/L = -0.65$, $h/\delta = 11.87$ for SARC and $h/\delta = 14.11$ for $k-\omega$ SST, meaning SARC predicts a thicker boundary layer. SARC and SA predict similar incoming boundary layer thicknesses even though they display many differences further downstream because upstream there is no curvature, so the curvature correction term is small. The experimental boundary layer thickness was $h/\delta = 12.0$, therefore SARC is much closer to the experimental measurements than $k-\omega$ SST. The Reynolds number based on the momentum thickness, Re_θ, is a much less sensitive parameter than the boundary layer thickness and, at the measurement location, $Re_\theta = 2.59 \times 10^3$ for SARC and $Re_\theta = 2.53 \times 10^3$ for $k-\omega$ SST. The experimental value was $Re_\theta = 2.64 \times 10^3$, so once again SARC is closer. The inflow length in the simulations was tuned to match the experiments using SARC, so this result it expected. Though the Re_θ values vary slightly between each turbulence model, the results indicate good agreement of the incoming flow between the models and experiments.

The skin friction coefficient along the streamwise and spanwise centerlines from the simulations are shown in Fig. 4.11 and 4.12. The skin friction coefficient along the streamwise centerline is very dependent on the turbulence model. The first important takeaway is that SARC, SA and $k-\omega$ SST all predict separation, but none of the $k-\epsilon$ models separate. Experimental flow visualizations indicate separation, especially at the highest Reynolds number. The other three models do predict separation, but the separation and reattachment location vary. SARC separates first, immediately followed by $k-\omega$ SST and SA. SA and $k-\omega$ SST reattach at a similar location, followed further downstream by the reattachment of SARC. Thus, the separated region for SARC is predicted to be the largest, followed by $k-\omega$ SST and then SA. Both SARC and $k-\omega$ SST used curvature corrections and SA did not, which

	Turbulence model	z^+_{min} in BL	z^+_{min} on bump peak	y^+_{min} on sidewall	$Re_\theta(x10^{-3})$	h/δ
Sims.	SARC	0.0622	0.4544	0.099	2.59	11.87
	SA	0.0662	0.4711	0.099	2.59	11.78
	$k-\omega$ SST	0.0619	0.4455	0.0985	2.53	14.11
	$k-\epsilon$ LEBM	0.0635	0.4648	0.1012	2.49	13.82
	$k-\epsilon$ Standard Two-Layer	0.063	0.4703	0.1002	2.68	12.35
	$k-\epsilon$ Realizable Two-Layer	0.0611	0.453	0.0973	2.56	13.4
Exps.	-	-	-	-	2.64	12.0

Table 4.2: Flow and simulation characteristics for the turbulence model sensitivity simulations, compared to the experimental results at the same Re_L. The grid used in all of these cases was the fine grid with $338 \times 312 \times 150$ grid points. $Re_L = 3.41 \times 10^6$, which corresponds to a freestream velocity of 60 m/s.

implies that the curvature correction has a significant impact on the predicted size of the separated region for curved geometry. Since the pressure coefficient results suggest that SARC matches the experimental data slightly better than SA, it can be inferred that the larger separated region predicted by SARC is also more accurate to the actual flow. In summary, these results suggest that predicting the separation and reattachment location is very difficult for the turbulence models.

Fig. 4.11 and 4.12 also show that the different turbulence models predict different maximum values of the skin friction coefficient over the top of the bump. Disregarding the $k-\epsilon$ models, SA predicts the highest value over the top of the bump and $k-\omega$ SST predicts the lowest maximum.

The streamwise pressure coefficients are shown in Fig. 4.13, with a close-up of the pressure coefficient in the separated region along the streamwise centerline shown in Fig. 4.14. Fig. 4.15 shows the spanwise centerline pressure coefficients.

Outside of the separated region all of the turbulence models show nearly perfect agreement with each other, and good agreement with the experimental dataset. There is a discrepancy with the pressure coefficient at the peak of the bump between the turbulence models, which all predicted a value of about -1.4, and the experiment, which predicted the minimum pressure to be about -1.2. The simulations correspond closely from X/L = 0.5 to end of the domain, but only agree with the experiments from X/L = 1 to the end of the domain.

Within the separated region, the turbulence model results diverge from each other and from the experiments. Fig. 4.14 shows that, while none of the turbulence models follow the data well, the closest are SARC and $k-\omega$ SST, because they both display a slight inflection point around X/L = 0.1. This result was expected due to the inclusion of the curvature correction in these two models. The other four turbulence models have smooth profiles throughout the entire region.

Looking at the spanwise centerline shows that none of the turbulence models have the double peaked profile, which is seen in the experiments. The simulations do a good job matching the experiment at the shoulders of the bump and tapering towards the wall, but

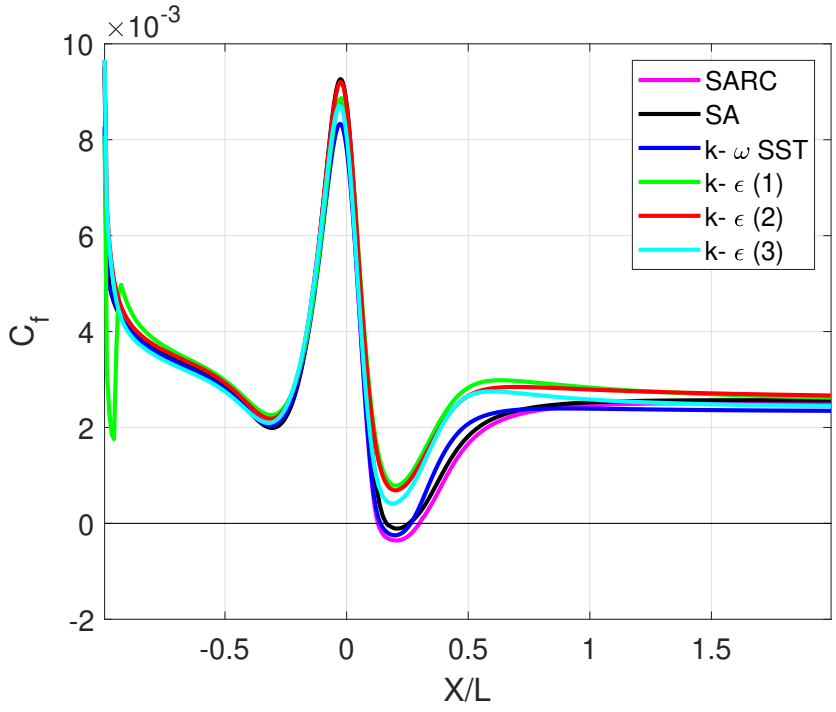

Figure 4.11: Variation in skin friction coefficient along the streamwise centerline. All simulations and experiments conducted at $Re_L = 3.41 \times 10^6$ (60 m/s) and $H/L = 1/2$.

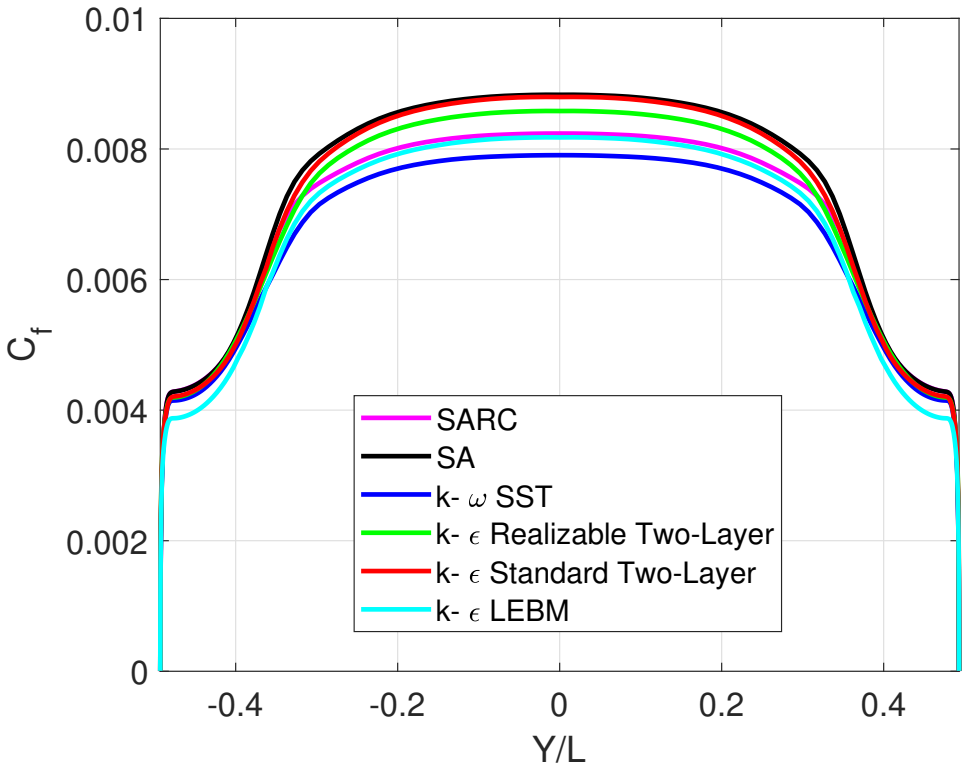

Figure 4.12: Skin friction coefficient along along the ridge of the bump ($x = 0$). All simulations and experiments conducted at $Re_L = 3.41 \times 10^6$ (60 m/s) and $H/L = 1/2$.

they fail across the top of the bump, incorrectly predicting both the profile shape and the pressure coefficient minimum values.

4.2.2 Confinement

The influence of flow confinement on surface pressures was examined in a series of experiments. Five velocities were tested at stations 4, 3, 2 and 1, which correspond to vertical positions of H/L = $1/2, 5/12, 1/3, 1/4$. Fig. 4.16 shows the pressure coefficient for all of the taps for stations 1, 2, 3 and 4 at the highest Reynolds number. Fig. 4.17, 4.18 and 4.19 show the streamwise and spanwise centerlines for the same data. The plots for the other velocities are not included in this thesis because the trends are the same as in the 60 m/s case. Error bars have not yet been determine for this set of results.

These plots show that, with increased confinement, the pressure magnitudes increase in most cases, consistent with faster flow speeds over the bump and stronger pressure gradients. The increase is the largest over the top of the bump. At station 4, the pressure coefficient at the bump peak is about -1.2, and at station 1, it is about -1.7. The plot of the streamwise centerline shows that in the separated region, the increase in pressure coefficient between stations 2 and 1, the most confined case, is the most significant change. This jump is almost double the jump from station 4 to station 2.

The asymmetry that can be seen between tap pairs in Fig. 4.16, such as taps 21/22, 25/26, 27/28 etc., appears to get worse for the more confined cases. As previously noted, the reason for this asymmetry has not yet been identified. The spanwise centerline in Fig. 4.19 shows that the double-peaked profile appears at every level of confinement. The increasing asymmetry between the taps on either side of the center tap, which was observed in Fig. 4.16, is also evident here.

4.3 Surface Flow Visualization

Surface contours of pressure and skin friction coefficients and surface streamlines were plotted from the simulation data to investigate the sensitivity to Reynolds number and turbulence

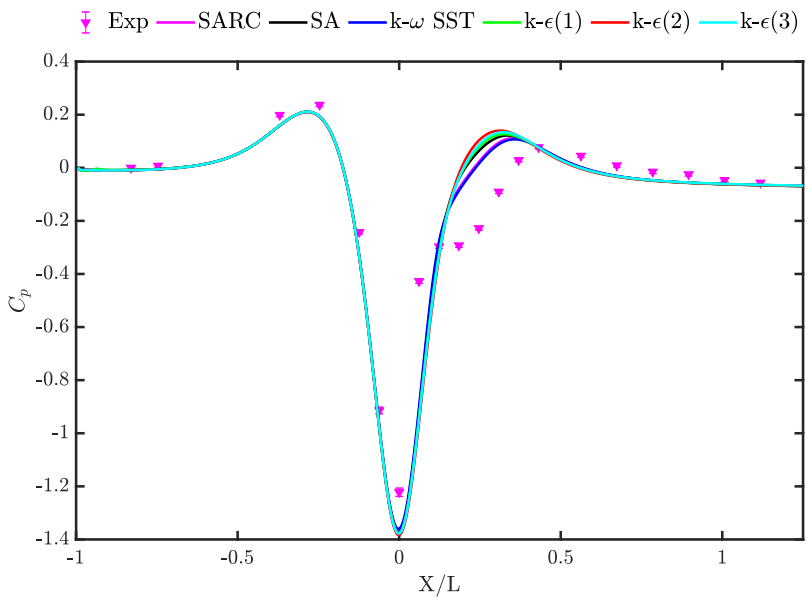

Figure 4.13: Variation in pressure along the streamwise centerline for turbulence model sensitivity studies (data shown in solid lines). All simulations conducted at $Re_L = 3.41 \times 10^6$ (60 m/s) and $H/L = 1/2$. Simulation data compared to experimental data at same vertical position and Reynolds number (shown in points).

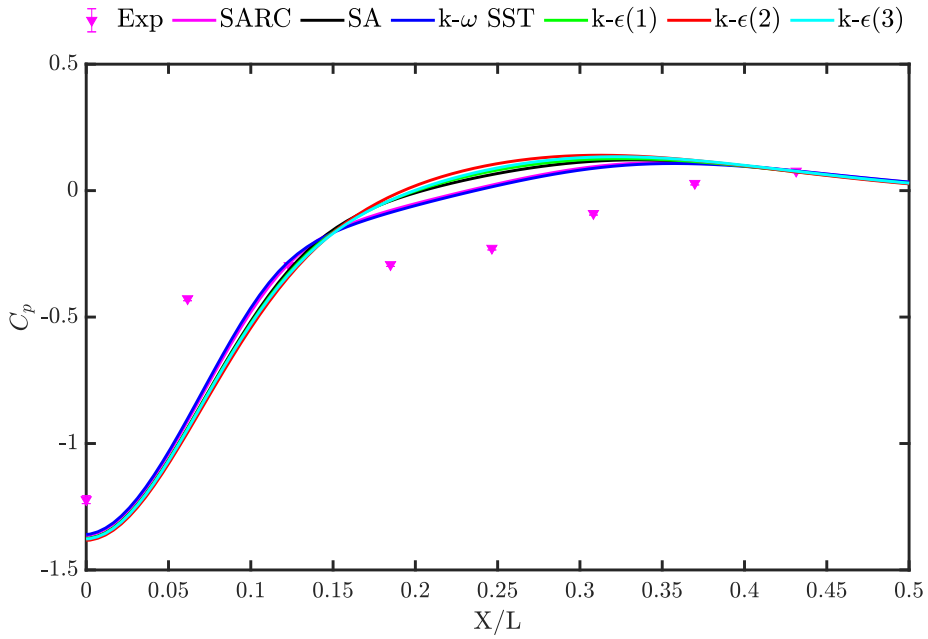

Figure 4.14: Highlighting the separated region shown in Fig. 4.13. All simulations conducted at $Re_L = 3.41 \times 10^6$ (60 m/s) and $H/L = 1/2$.

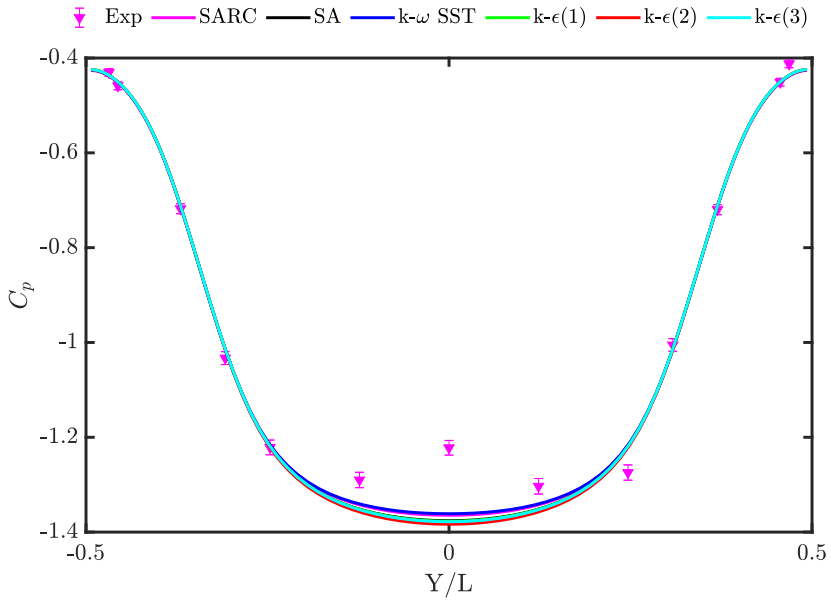

Figure 4.15: Spanwise centerline. Cases same as in Fig. 4.13. All simulations conducted at $Re_L = 3.41 \times 10^6$ (60 m/s) and $H/L = 1/2$.

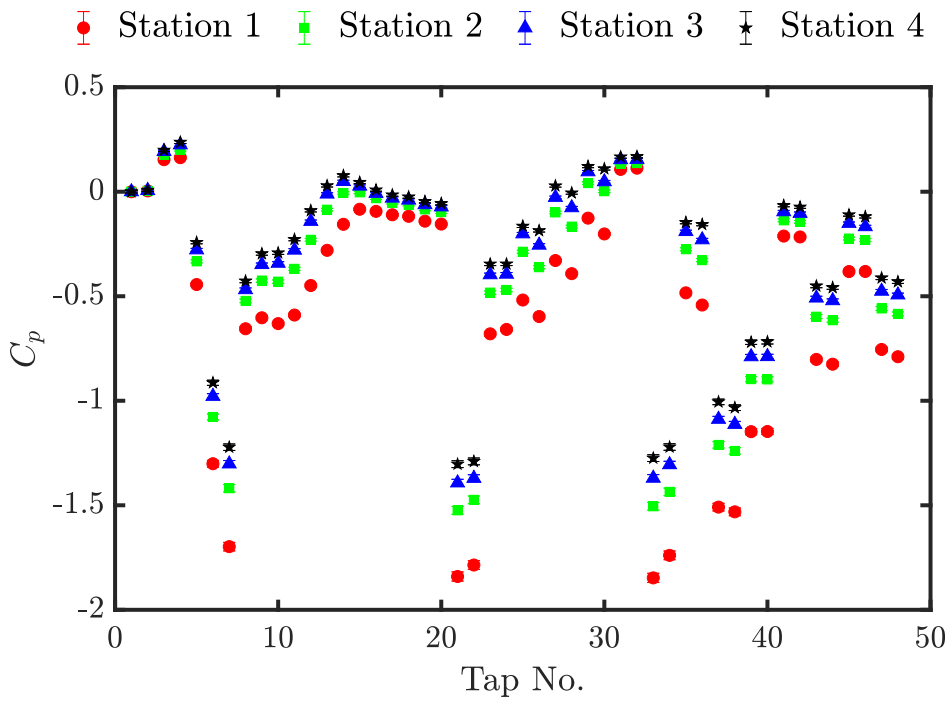

Figure 4.16: Survey of all experimental pressure coefficient data for vertical positions H/L = $1/2, 5/12, 1/3, 1/4$ (stations 4, 3, 2, and 1) at $Re_L = 3.41 \times 10^6$ (freestream velocity of 60 m/s). Tap numbers correspond to locations in Figure 3.5.

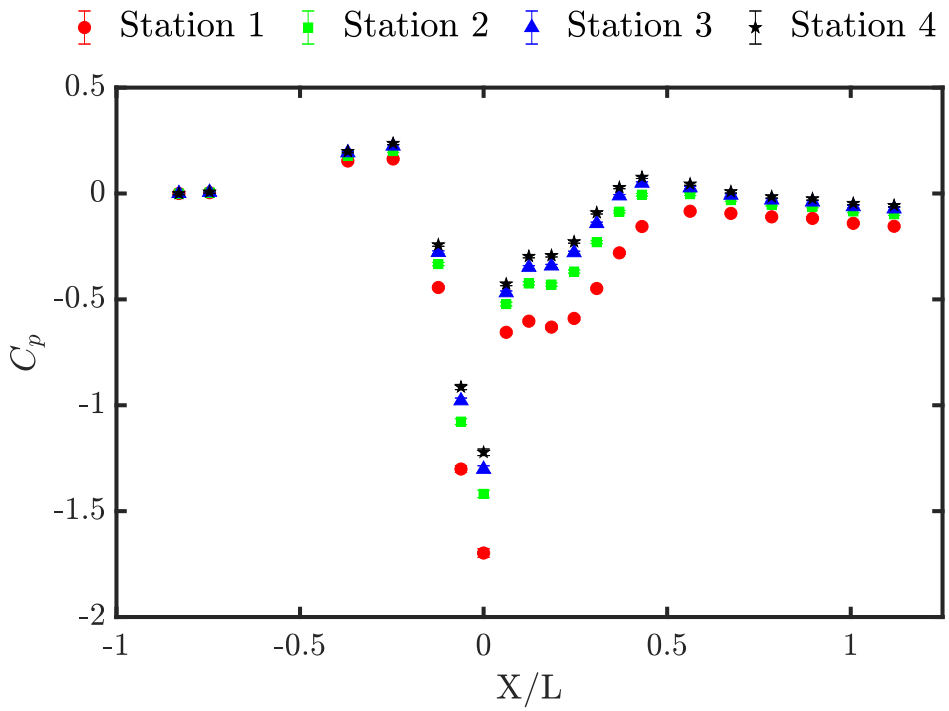

Figure 4.17: Pressure coefficient along the streamwise centerline for vertical positions H/L = $1/2, 5/12, 1/3, 1/4$ (stations 4, 3, 2, and 1) at $Re_L = 3.41 \times 10^6$ (freestream velocity of 60 m/s).

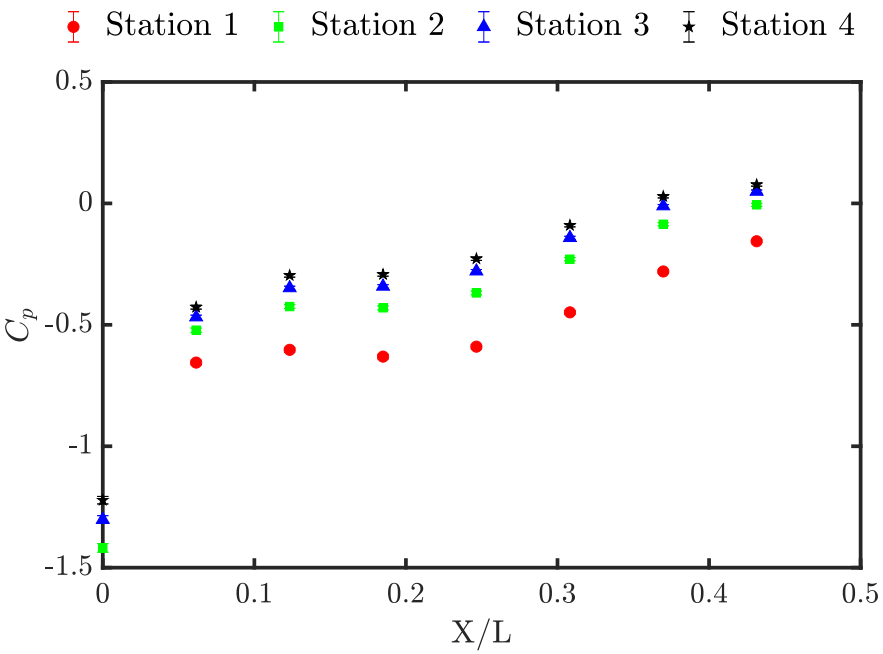

Figure 4.18: Highlighting the separated region shown in Fig. 4.17. Vertical positions H/L = $1/2, 5/12, 1/3, 1/4$ (stations 4, 3, 2, and 1) at $Re_L = 3.41 \times 10^6$ (freestream velocity of 60 m/s).

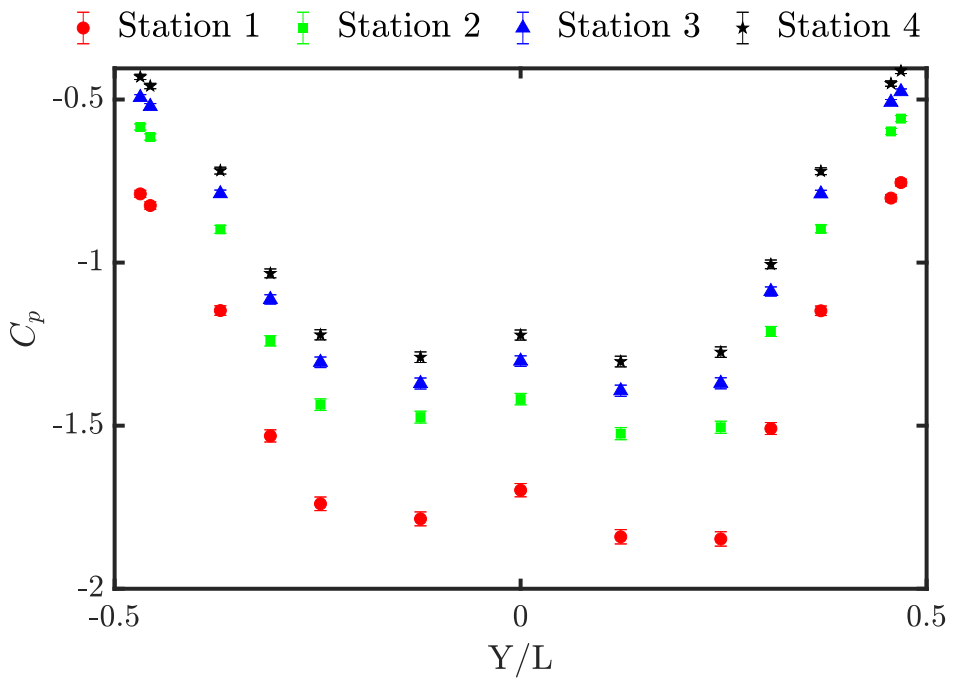

Figure 4.19: Variation in pressure along the ridge of the bump ($x = 0$). Cases as in Figure 4.17. Vertical positions $H/L = 1/2, 5/12, 1/3, 1/4$ (stations 4, 3, 2, and 1) at $Re_L = 3.41 \times 10^6$ (freestream velocity of 60 m/s).

model. The surface streamline data was compared to experimental flow visualizations.

The pressure and skin friction coefficients for SARC at 60 m/s, 40 m/s, 30 m/s and 20 m/s are shown in Fig. 4.20. The 50 m/s contour was excluded because it fell equally between the 60 m/s and 40 m/s plots, which have been included. The flow direction in this plot is from the left hand side of the page to the right. The top of the bump is shown by the blue region in the pressure coefficient plot and the red region in the skin friction coefficient plot. In these contour plots, red represents positive values, blue is negative and white is zero. The separated region is most clearly seen in the skin friction coefficient plot because it is where the skin friction becomes zero. The separation line downstream of the spanwise centerline looks similar for all Reynolds numbers, but the reattachment point looks different. At 60 m/s, the reattachment line is a smooth curve, but at the lower velocities, a kink appears in the curve at the streamwise centerline, suggesting that flow along the streamwise centerline takes slight longer to reattach then the rest of the flow. Moreover, the skin friction in the separated region becomes more negative for the lower Reynolds number cases. The pressure coefficient plot shows that, except for 60 m/s, the rest of the cases have two higher pressure spots in the separated region, which are symmetric to the streamwise centerline. The pressure and skin friction coefficient contours support the conclusion that the geometry is not insensitive to Reynolds number, especially at the lower velocities.

Pressure and skin friction coefficient contours for SARC, SA and $k-\omega$ SST are shown in Fig. 4.21. The results for the $k-\epsilon$ models are not included because none of them produced a separated flow. The skin friction coefficient plots reaffirm the conclusions made based on the streamwise and spanwise skin friction coefficient plots, namely that SARC predicts the largest separated region. However, in these contours it seems as though the separated regions in SA and $k-\omega$ are about the same size in the streamwise direction, but SA predicts a slightly wider separated region.

The region of the maximum pressure coefficient in the separated region of both SARC and $k-\omega$ SST have a reverse kidney shape, while the same region in the SA results does not have that curved shape. This could be a difference between models that use a curvature

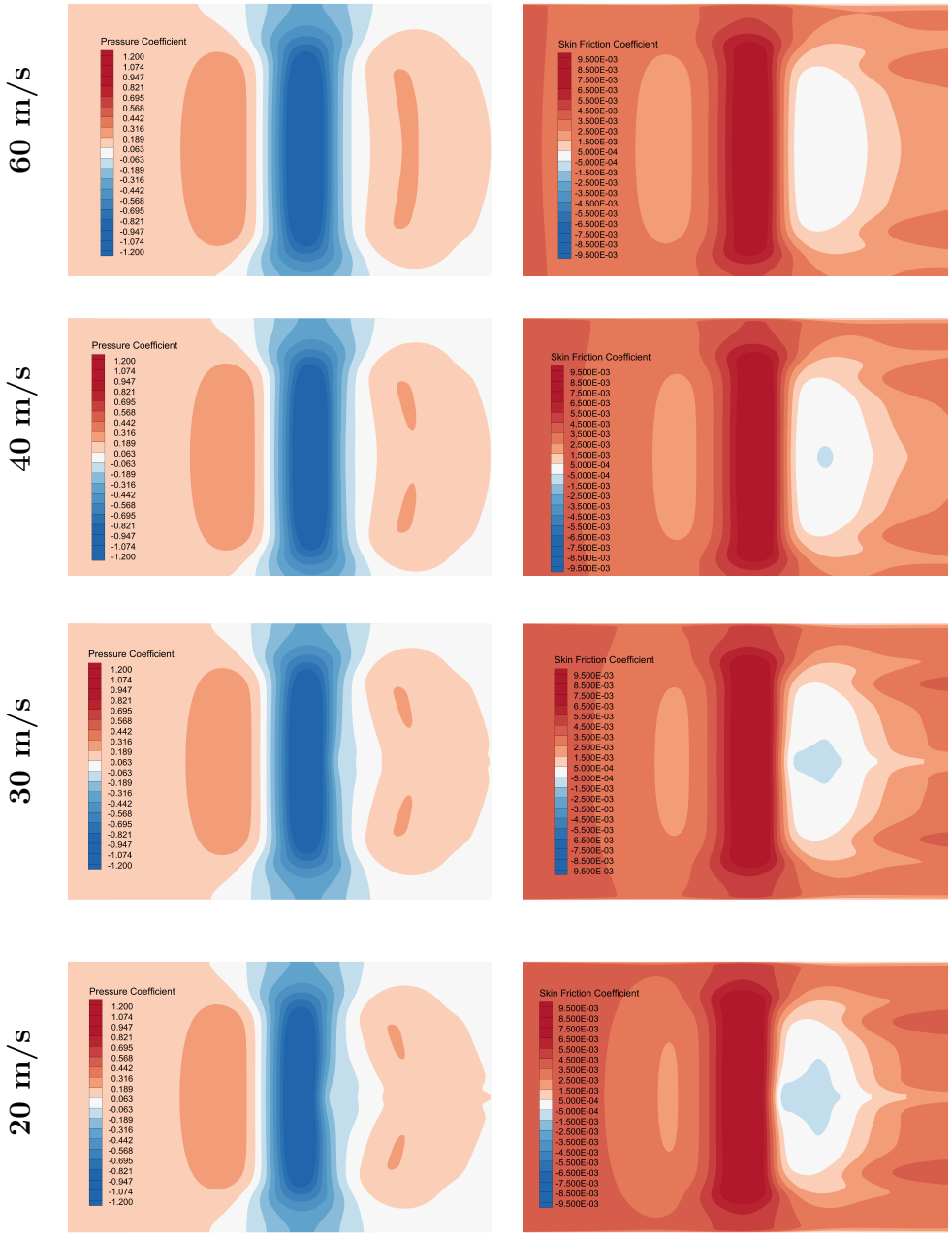

Figure 4.20: Top down view of pressure and skin friction coefficients contours for SARC with varying freestream velocity (Re_L). The streamwise direction is horizontal across the page, the bump is visible in blue on the pressure plot and red on the skin friction plot. Upstream is to the left and downstream to the right. Red corresponds to positive values, blue to negative and white to zero.

correction (SARC and $k-\omega$ SST) and the one that does not (SA).

Surface streamline plots were developed from the simulations using the wall shear stress and plotted over the pressure coefficient contours. These streamline plots were compared with surface flow visualizations that were done using the china clay method. This work was conducted by Sage Sarwas and discussed in their Master's thesis [25].

Fig. 4.22 compares the flow visualization for a freestream velocity of 60 m/s to a surface streamline plot from a simulation that used SARC, with a freestream velocity of 60 m/s. The image shows the downstream side of the bump and the flow direction is from the top of the image to the bottom. The spanwise and steamwise centerlines are shown by the red dashed line in the experimental image. The image from the experiments indicates the presence of two counter-rotating vortical structures in the separated region on either side of the streamwise centerline. Pooling of the mixture in the separated region, particularly in the vortices, occurred at all velocities, but worsened for the lower velocities, meaning that most of the structures within the separation and reattachment regions are blurred. The comparison at 60 m/s is the clearest of all the velocities because it has the least amount of pooling. At 60 m/s, the separation line can clearly be seen at the top of the image, slightly downstream of the spanwise centerline. Reattachment occurs the saddle point, which is downstream of the vortical structures and located on the streamwise centerline.

Surface streamlines were also plotted using the data from the CFD simulations to determine whether the same structures are visible in the simulations and the experiments. The streamlines are plotted over the pressure coefficient contours, which was also shown in Fig. 4.21. The surface streamlines shown in Fig. 4.22 are for the SARC case at the same Reynolds numbers as the experimental images. These same general structures are visible in the computational streamlines. In the simulations, the separation line is predicted slightly farther downstream from the spanwise centerline than where the flow appears to separate in the experiments. The saddle point is also clear in the streamlines, however, it might be farther upstream than it was in the experiments, meaning that is seems like the RANS-SARC simulations predicted a smaller separated region that what was seen in the wind tunnel.

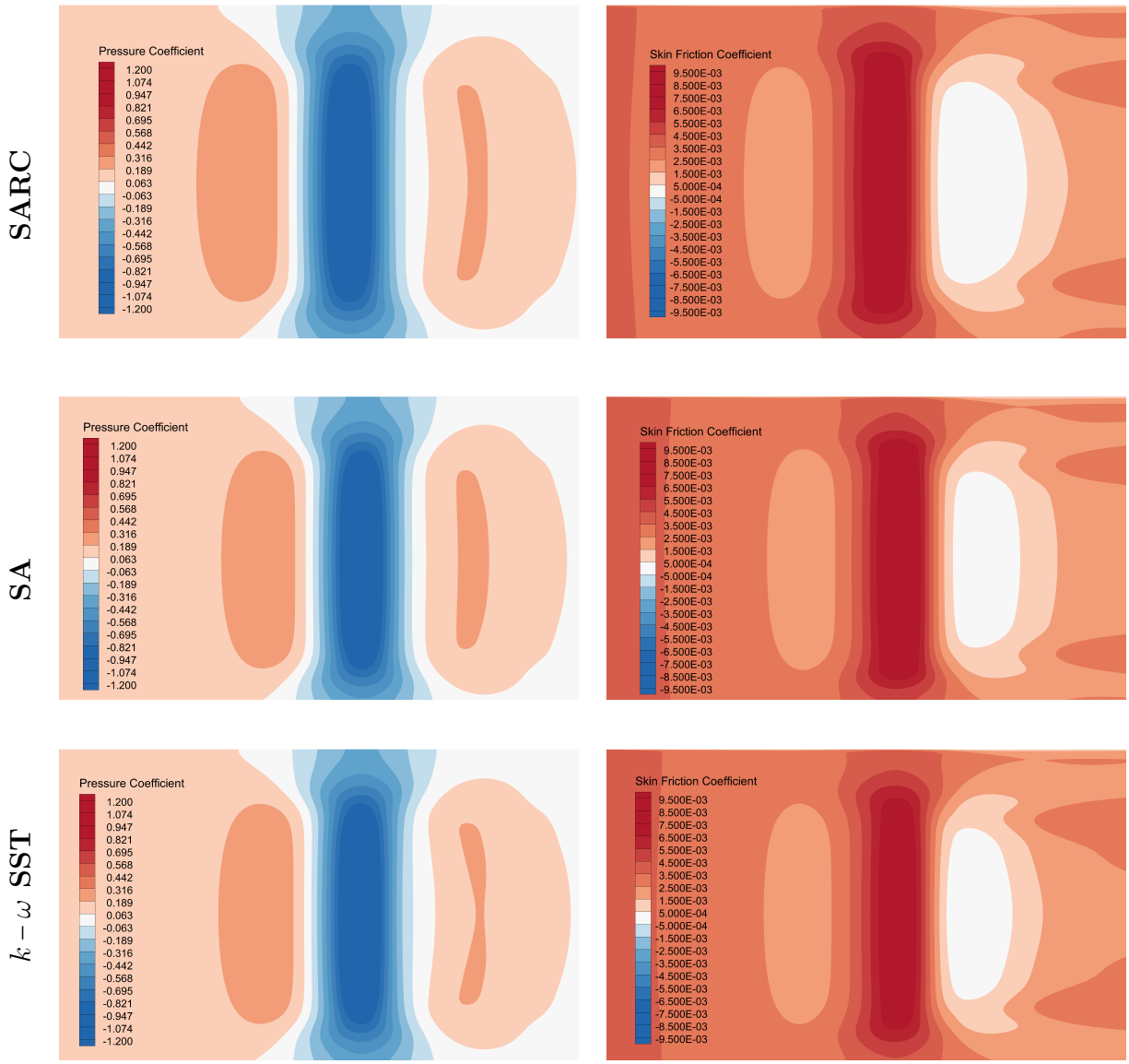

Figure 4.21: Top down view of pressure and skin friction coefficient contours for $Re_L = 3.41 \times 10^6$ for SARC, SA and $k-\omega$ turbulence models. The streamwise direction is horizontal across the page, the bump is visible in blue on the pressure plot and red on the skin friction plot. Upstream is to the left and downstream to the right. Red corresponds to positive values, blue to negative and white to zero.

Futhermore, it appears as though the simulation separated region is wider than the experimental one, as it spans almost the whole width of the bump. Finally, the surface vortices that dominated the separated region in the experiments [26] seem to be closer to the centerline in the experimental flow than in the simulations, though they are still symmetric to the streamwise centerline.

Fig. 4.23 shows a comparison between an experimental and computational visualization of the surface streamlines for the same level of confinement with a freestream velocity of 30 m/s. The SARC turbulence model was used for the simulation shown. The streamlines at this Re_L appear to match less well than the streamlines at the higher Re_L case. The simulation results predict that the separated region is larger for the 30 m/s case than for 60 m/s. Furthermore, in the 60 m/s case, the separation line was straight across the top of the separated region. In the 30 m/s case, there is a peak in the middle, indicating that the flow separates first along the streamwise centerline and separation occurs slightly farther downstream in the flow that is closer to the sidewalls. This peak was not so clear in the 60 m/s case in Fig. 4.22, where the separation line did not exhibit a clear peak, but rather a smooth curve. This feature is visible in both the experimental and simulation result.

The streamline results were also plotted for the $Re_L = 3.41 \times 10^6$ simulations using the SA and $k-\omega$ SST turbulence models. None of the $k-\epsilon$ results were included because that turbulence model never produced separation. These were plotted alongside the $Re_L = 3.41 \times 10^6$ SARC plot, which was discussed previously and included in Fig. 4.22.

All of the plots show separation occurring downstream of the spanwise centerline and the saddle point occurs on the streamwise centerline further downstream. The size and shape of the separation bubble, as well as the separation and reattachment locations, vary between the three turbulence models. The largest separation bubble is predicted by SARC. It predicts the farthest upstream separation point and the farthest downstream reattachment point. It also predicts the widest separation bubble. The SA separation point is significantly farther downstream and the reattachment point is more upstream, leading to a thinner streamwise separated region. The separated region also appears to be slightly narrower in the spanwise

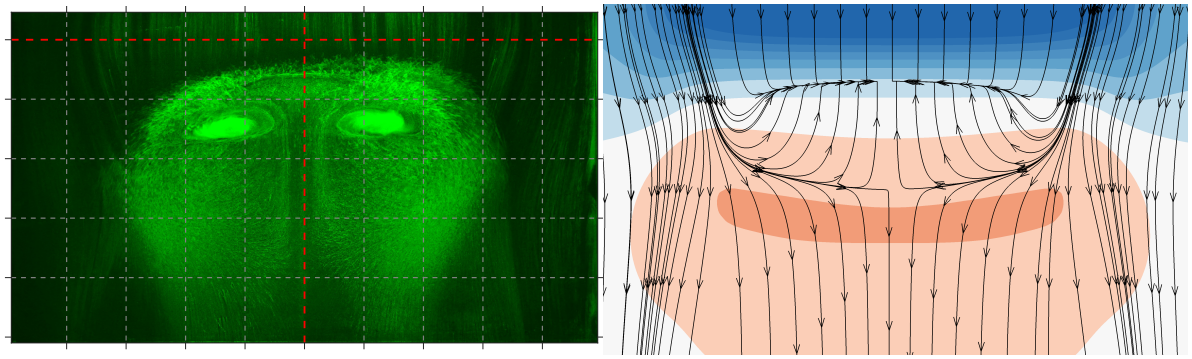

(a) (b)

Figure 4.22: (a) Surface flow visualization using the china clay method at $Re_L = 3.41 \times 10^6$, which corresponds to 60 m/s in the UW 3' x 3' wind tunnel. The centerline of the bump in both streamwise and spanwise directions is indicated with red dashed lines. (b) Simulation surface streamlines for the same case with the SARC turbulence model, laid over a rotated version of the pressure coefficient contour for SARC and 60 m/s shown in Fig. 4.20 and 4.21. Here the streamwise direction is vertical with upstream at the top of the image and downstream at the bottom.

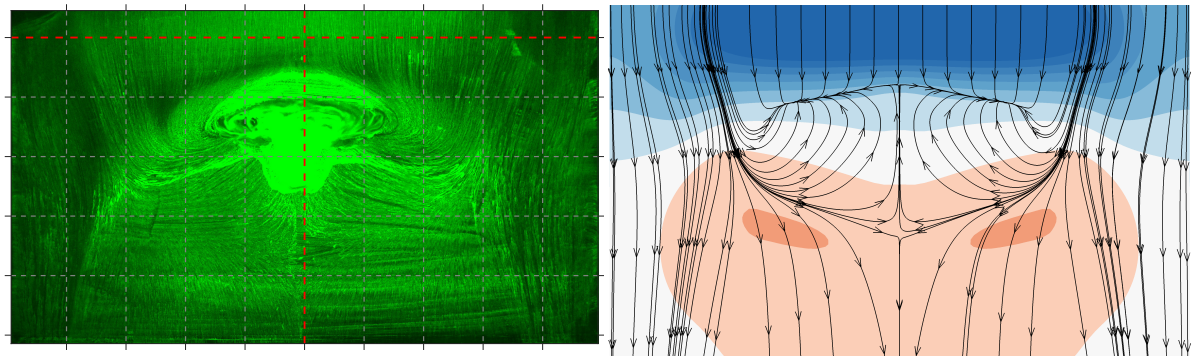

(a) (b)

Figure 4.23: (a) Surface flow visualization using the china clay method at $Re_L = 1.87 \times 10^6$, which corresponds to 30 m/s in the UW 3' x 3' wind tunnel. The centerline of the bump in both streamwise and spanwise directions is indicated with red dashed lines. (b) Simulation surface streamlines for the same case with the SARC turbulence model, laid over a rotated version of the pressure coefficient contour for SARC and 30 m/s shown in Fig. 4.20. Here the streamwise direction is vertical with upstream at the top of the image and downstream at the bottom.

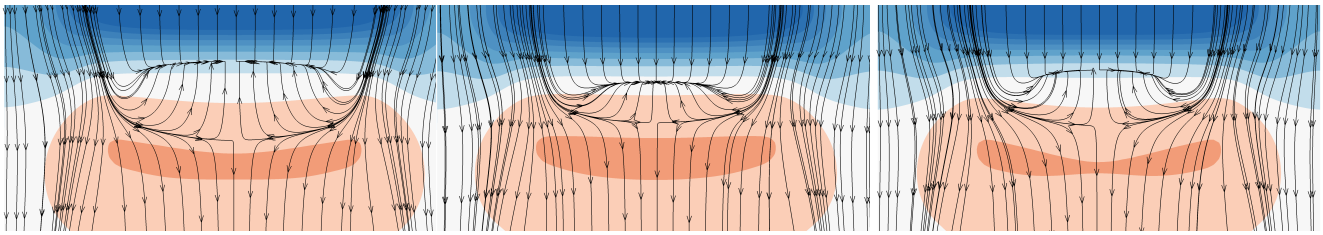

(a) (b) (c)

Figure 4.24: Surface streamlines from CFD simulations for the following turbulence models: (a) SARC (b) SA (c) $k-\omega$ SST. All simulations were conducted at $Re_L = 3.41 \times 10^6$ (60 m/s). Streamlines overlaid onto rotated versions of the pressure coefficient contours shown in Fig. 4.21. Here the streamwise direction is vertical with upstream at the top of the image and downstream at the bottom.

direction. The separation bubble predicted by $k-\omega$ SST seems to fall in between the two, both in respect to location of separation and the streamwise width. It appears that the reattachment point predicted by $k-\omega$ SST is at about the same location at the reattachment point for SA. Additional streamline contours are included in Appendix A.

Chapter 5

CONCLUSION

The research in this thesis was conducted in support of a larger project that aims to fulfill the needs stipulated in the "CFD Vision 2030" report. Namely, to produce a validation test case for turbulent separated flow and simultaneously investigate current RANS models using the same geometry chosen for the experimental validation. The speed-bump-like geometry that was chosen is Gaussian along the streamwise centerline and uniform in the spanwise direction until it tapers down at the sidewalls. The geometry is a smooth curve, therefore it does not have a geometrically fixed separation point. It is also tapered to minimize sidewall interactions. Research on this project, presented at the SciTech 2020 Forum, concluded that some three-dimensionality is present at the streamwise centerline [26]. This thesis builds upon initial work done by graduate student Sage Sarwas [25], as well as the research presented at Scitech 2020 in Orlando, Florida [26]. The goal of this thesis was to use a combination of experiments and simulations to determine if the bump geometry is a stringent test of current RANS turbulence models, examine the sensitivity of the flowfield to Reynolds number and confinement and identify the regions or features of the flow that seem most different between common RANS turbulence models. The tests conducted include surface pressure measurements, incoming boundary layer measurements, surface flow visualizations comparisons, and tests at various Reynolds numbers, levels of flowfield confinement and using various RANS turbulence models.

The Reynolds number based on the momentum thickness, Re_θ, and the boundary layer thickness, δ, from the experiments and the simulations were compared at the measurement location. Originally, this comparison was conducted for the simulations using Spalart-Allmaras with a curvature correction (SARC), but the other turbulence models examined, standard

Spalart-Allmaras (SA), $k-\omega$ SST with a curvature correction, and the $k-\epsilon$ models (lag elliptic blending model, standard two-layer and realizable two-layer) also had similar inflow profiles. Re_θ corresponded particularly well between all models and the experiments. Evidence supporting this similarity is shown in Table 4.1, 4.2 and boundary layer plots shown in Fig. 4.1. Proving that the inflow matched was important to ensure that comparisons between experiments and simulations in the separated region were valid.

Simulations predicted opposite surface pressure Reynolds number trends in the separated region to what was measured in the experiments. Moreover, two profiles were observed in the experimental pressure coefficient measurements, an inflection point in the separated region along the streamwise centerline and a double peak across the bump peak. While these profiles were observed at all Reynolds numbers in the experiments, they were only observed in the SARC simulations at the two lowest Reynolds numbers. Finally, comparisons between the surface streamlines and experimental surface flow visualizations show that, though the separated regions predicted by the simulations and seen in the experiments predict different widths and separation and reattach locations, they do have the same general shape and they both contain the counter-rotating surface vortices on either side of the streamwise centerline. Therefore, the bump geometry was determined to be a stringent test of current RANS models because there is clear discrepancy between the simulations and the experiments in the separated region, even though the data in the attached regions are very similar.

Previous experiments [25, 26] concluded that the flowfield was insensitive to Reynolds number above $Re_L = 2.4\times10^6$. Current RANS simulations were also seen to be approximately insensitive above the same Reynolds number. The simulations also concluded that the size of the separated region decreases with increasing Reynolds number.

From the tests that were conducted with various levels of vertical confinement, it was found that increasing the confinement increases the magnitude of the pressure throughout the flowfield. The pressure coefficient at the peak of the bump was about -1.2 for the least confined case and about -1.6 for the most confined case. No new trends in the data were observed and the shape of the pressure coefficient profiles remained the same.

Simulations were conducted using SARC, SA, $k-\omega$ SST and three versions of $k-\epsilon$, but none of the $k-\epsilon$ predicted separation. Experimental pressure coefficient profiles were seen to be much more accurately predicted by RANS models with curvature corrections, SARC and $k-\omega$ SST. This suggests that using a curvature correction on a curved geometry has a significant effect on the results. From the surface streamline comparisons, it is clear that the separated regions vary in size between SARC, SA and $k-\omega$ SST, with SARC being the largest and SA the smallest. The width, separation point and reattachment point are not the same between the three models, but those three models did each predict a separated region that was symmetric across the streamwise centerline and featured two counter-rotating surface vortices.

Evaluation of this validation geometry for turbulent separated flow will continue. Further RANS simulations will investigate the influence of flow confinement and comparisons with experimental confinement sensitivity data.

On the experimental side, particle image velocimetry (PIV) measurements of this flowfield will be conducted. They will enable a more in-depth understanding of the experimental flow and allow for a more direct comparison to the simulation results by providing measurements and visualization of the complete flowfield. The turbulence kinetic energy (TKE) can be calculated from PIV measurements, which can be used to compare more directly to the simulations and inform the development and improvement of RANS models for turbulent separated flow.

Additionally, the intent is to reach a completeness level 2, outlined by Oberkampf and Smith [8] in all six validation readiness categories. Some steps to reach this goal include rigorous uncertainty analysis on all experimental data, inflow measurements to determine the flow uniformity in the 3'x3' wind tunnel where all experimental work is conducted, and a three-dimensional scan of the physical bump to determine any discrepancies between it and its mathematical definition. The goal is for this UW-Boeing collaboration to result in a high-quality validation test case for turbulent separated flow and help improve and advance the field of computational fluid dynamics and its efficacy in the aerospace industry.

REFERENCES

[1] Leschziner, M. A., "Modelling turbulent separated flow in the context of aerodynamic applications," *Fluid Dynamics Research*, Vol. 38, No. 2-3, feb 2006, pp. 174–210.

[2] Greenblatt, D., Paschal, K., Schaeffler, N., Washburn, A., and Yao, C., "Separation control over a wall-mounted hump: A CFD validation test case," *AIAA Paper 2004-2219*, 2004.

[3] Bell, J., Heineck, J., Zillac, G., Mehta, R., and Long, K., "Surface and flow field measurements on the FAITH Hill Model," *AIAA-2012-0704*, 2012.

[4] Disotell, K. J. and Rumsey, C. L., "Design of an Axisymmetric afterbody test case for CFD Validation," *AIAA 2017-3792*, 2017.

[5] T. Lowe, C. Beardsley, A. B. W. D. J. D.-P. D. F. A. G. C. R. M. S. V. V., "Status of the NASA/Virgina Tech Benchmark Experiments for CFD Validation," *SciTech Forum*, 2020.

[6] Rumsey, C., Gatski, T., Sellers, W., Vatsa, V., and Viken, S., "Summary of the 2004 CFD Validation Workshop on Synthetic Jets and Turbulent Separation Control," *2nd AIAA Flow Control Conference*, 2004.

[7] Slotnick, J., Khodadoust, A., Alonso, J., Darmofal, D., Gropp, W., Lurie, E., and Marvriplis, D., "Vision 2030 CFD study: A path to revolutionary computational aerosciences," Tech. rep., NASA/CR-2014-218178, 2014.

[8] Oberkampf, W. L. and Smith, B. L., "Assessment Criteria for computational fluid dynamics validation benchmark experiments," *AIAA SciTech Forum*, 2014.

[9] Simpson, R. L., "Turbulent Boundary-Layer Separation," *Annual Review of Fluid Mechanics*, Vol. 21, No. 1, 1989, pp. 205–232.

[10] Simpson, R. L., C. Y. T. S. B. G., "The structure of a separating turbulent boundary layer. Part 1. Mean flow and Reynolds Stress," *Journal of Fluid Mechanics*, Vol. 113, 1981, pp. 23–51.

[11] Spalart, P. and Allmaras, S., "A One-Equation Turbulence Model for Aerodynamic Flows," *AIAA*, Vol. 439, 01 1992.

[12] Wilcox, D. C., "Formulation of the k-w Turbulence Model Revisited," *AIAA Journal*, Vol. 46, No. 11, 2008, pp. 2823–2838.

[13] Star-CCM+, "Star-CCM+ Documentation," Tech. rep., Siemens, 2016.

[14] Hanjalić, K. and Launder, B. E., "A Reynolds stress model of turbulence and its application to thin shear flows," *Journal of Fluid Mechanics*, Vol. 52, No. 4, 1972, pp. 609–638.

[15] Menter, F. R., "Zonal Two Equation $k-\omega$ Turbulence Models For Aerodynamic Flows," 1993.

[16] Driver, D., "Reynolds shear stress measurments in a separated boundary layer flow," *AIAA-1991-1787, 22nd Fluid Dynamics, Plasma Dynamics and Lasers Conference, Honolulu, HI*, 1991.

[17] Webste, D., DeGraaff, D., and Eaton, J., "Turbulence characteristics of a boundary layer over a swept bump," *Journal of Fluid Mechanics*, Vol. 323, 1996, pp. 1–22.

[18] Byun, G. and Simpson, R. L., "Structure of three-dimensional separated flow on an axisymmetric bump," *AIAA Journal*, Vol. 44, No. 5, 2006.

[19] Husen, N., Woodiga, S., Liu, T., and Sullivan, J., "Global luminescent oil-film skin friction meter generalized to three-dimensional geometry and applied to FAITH Hill," *AIAA SciTech Forum*, 2014.

[20] Bachalo, W. and Johnson, D., "Transonic turbulent boundary-layer separation generated on an axisymmetric flow model," *AIAA-1979-1479, AIAA 12th Fluid and Plasma Dynamics Conference, Williamsburg, VA*, 1979.

[21] Simmons, D., Thomas, F., and Corke, T., "Benchmark Smooth Body Flow Separation Experiments," June 2017.

[22] C. Beardsley, A. Gargiulo, T. O. V. V. D. F.-J. D.-P. M. S. A. B. K. L. C. R. W. D., "Computational Fluid Dynamic Analysis for the Assessment of Experimental Design Risks and Flow Sensitivities for a Three-Dimensional Bump Flow," *Aviation Forum*, 2020.

[23] Lynch, K. P., Barone, M. F., Beresh, S. J., Spillers, R., Henfling, J., and Soehnel, M., "Revisiting Bachalo-Johnson: The Sandia Axisymmetric Transonic Hump and CFD Challenge," *AIAA Aviation 2019 Forum*, 2019.

[24] R. Balin, K. Jansen, P. S., "Wall-Modeled LES of Flow over a Gaussian Bump with Strong Pressure Gradients and Separation," *Aviation Forum*, 2020.

[25] Sarwas, E. S., *Experimental examination of new separated turbulent flow validation test geometry*, Master's thesis, University of Washington, 2019.

[26] Williams, O. J., Samuell, M., Sarwas, S., Robbins, M., and Ferrante, A., "Experimental study of a CFD validation test case for turbulent separated flows," *SciTech Forum*, 2020.

[27] Roache, P. J., "Perspective: a method for uniform reporting of grid refinement studies," *Journal of Fluids Engineering*, Vol. 116, No. 3, 1994, pp. 405–413.

[28] Celik, I. B., Ghia, U., Roache, P. J., and Freitas, C. J., "Procedure for estimation and reporting of uncertainty due to discretization in CFD applications," *Journal of Fluids Engineering- Transactions of the ASME*, Vol. 130, No. 7, 2008.

[29] Matthew Robbins, M. S. and Williams, O. J., "Assessment of validation completeness for elongated-hill separated flow experiments," *SciTech Forum 2021*, (not yet published).

Appendix A

STREAMLINE CONTOURS

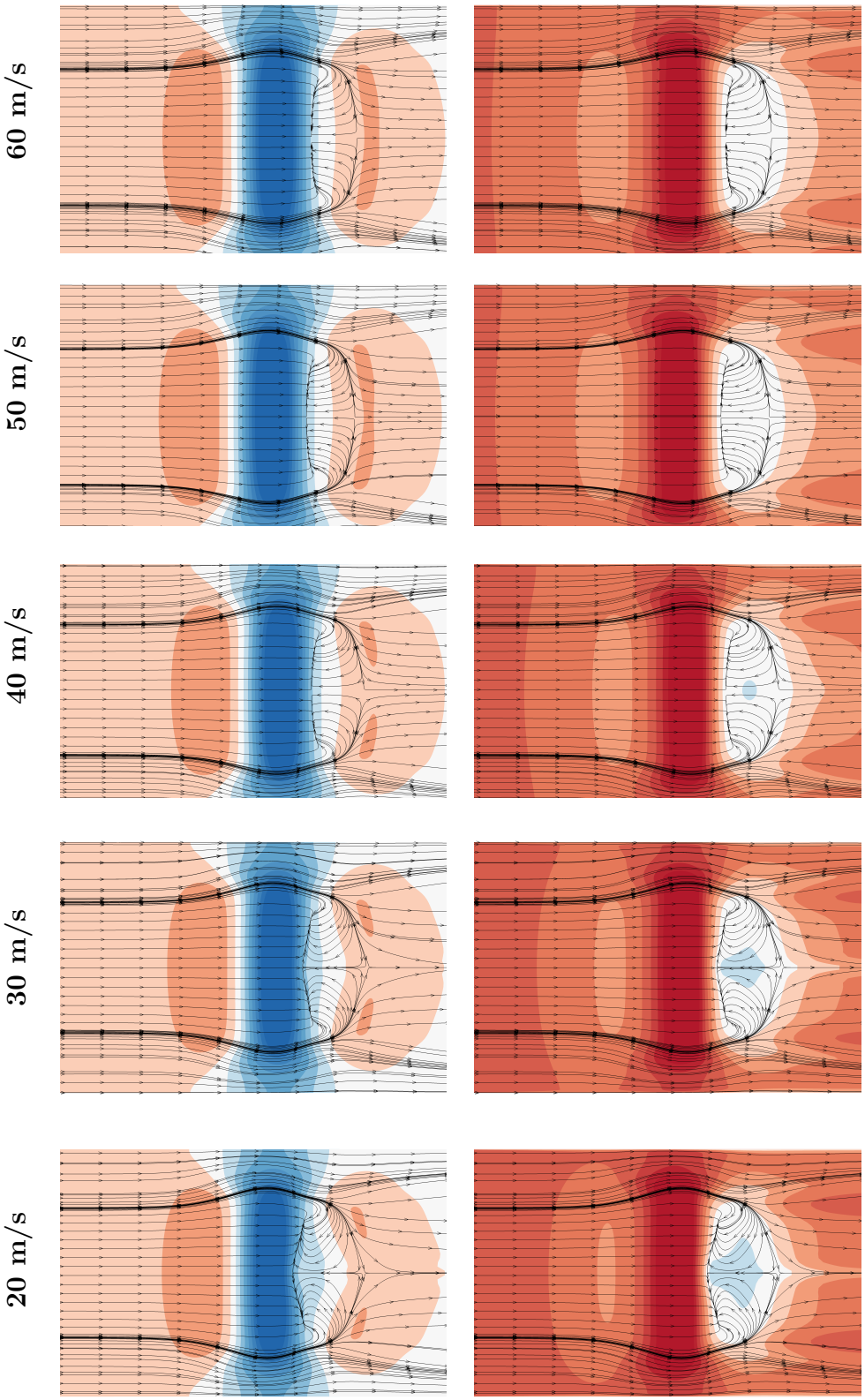

Figure A.1: Streamlines plotted over pressure and skin friction coefficient for all Reynolds numbers using SARC. Plate location at $H/L = 1/2$.

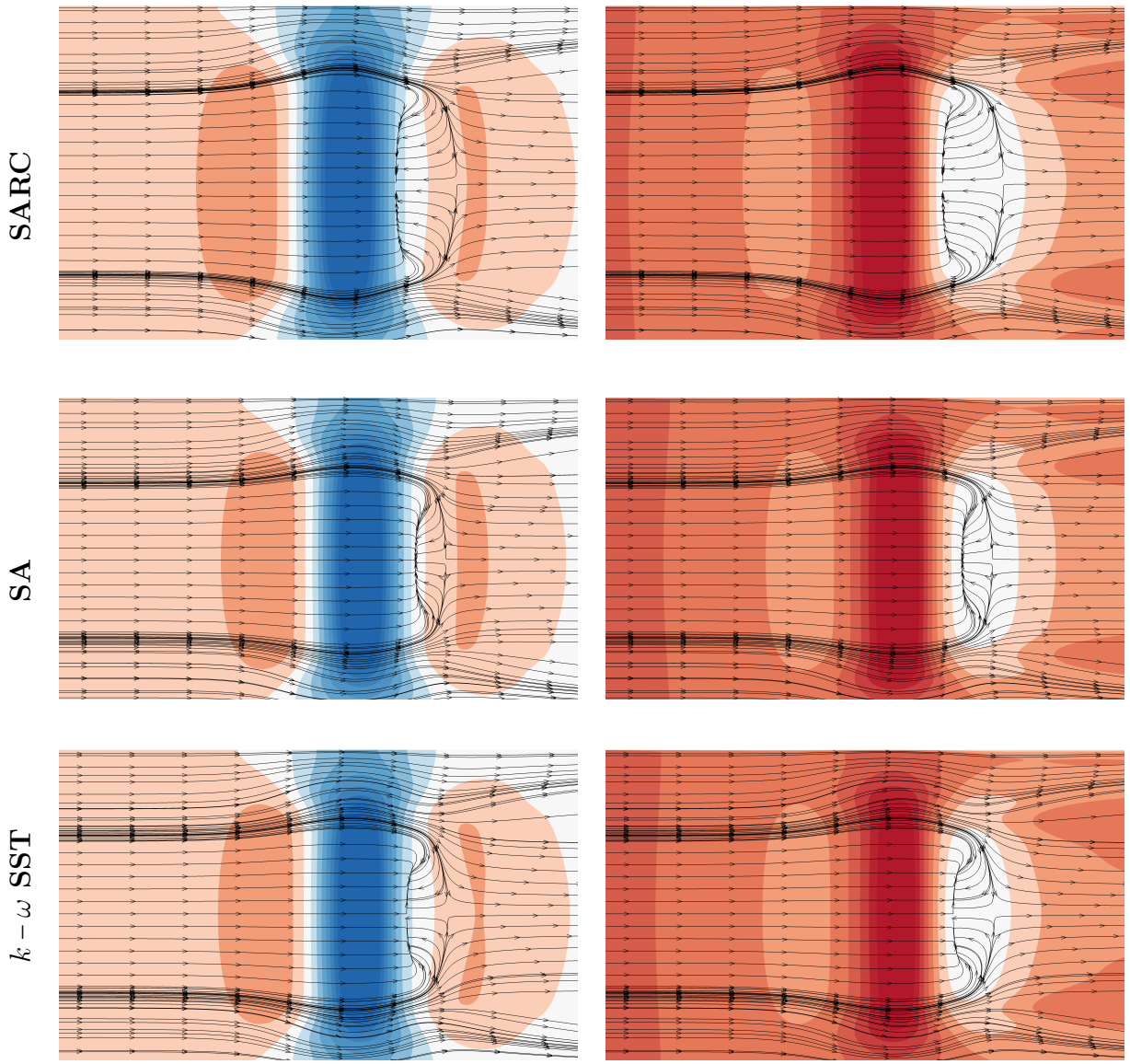

Figure A.2: Streamlines plotted over pressure and skin friction coefficient for all turbulence models at $Re_L = 3.41 \times 10^6$ (freestream velocity of 60 m/s). Plate location at $H/L = 1/2$.